# Hybrid Cathode for All-Solid-State Li-S Batteries

by

Shiqi Xu

A thesis

presented to the University of Waterloo

in fulfillment of the

thesis requirement for the degree of

Master of Science

in

Chemistry-Nanotechnology

Waterloo, Ontario, Canada, 2021

# AUTHOR'S DECLARATION

I hereby declare that I am the sole author of this thesis. This is a true copy of the thesis, including any required final revisions, as accepted by my examiners.

I understand that my thesis may be made electronically available to the public.

_____

Shiqi Xu

# ABSTRACT

Lithium-sulfur (Li-S) battery is one of the most promising energy storage candidates to satisfy the rising demands in multi-functional personal electronics, and the development of electric vehicles due to its high energy density and low cost. However, the commercialization of conventional Li-S batteries is subject to technical challenges, in which polysulfide shuttle is the most predominant as it often results in low columbic efficiency and poor capacity retention. The replacement of conventional liquid electrolyte with a solid-state electrolyte is the most effective solution to eliminate the polysulfide shuttling – albeit development of complex cathode host to retain polysulfide – since these lithium polysulfides cannot dissolve in the solid electrolyte. The all-state-state Li-S system may be the ultimate solution for commercializing Li-S cell technology. In this thesis, research was carried out to find new cathode host materials for solid-state Li-S batteries. Vanadium disulfide ($VS_2$) in particular features excellent electronic conductivity, enabling the material to have great potential to replace the traditional carbon black additives in the cathode composite. Therefore, metal sulfides were studied as cathode host materials in a solid-state Li-S cell. The performance of metal sulfide cathodes using different fabrication methods and morphologies was also investigated. This thesis encompasses two projects.

In my first project of this thesis, I reported an intercalation-conversion hybrid cathode that combines intercalation-type $VS_2$ with conversion-type sulfur to construct high performance solid-state lithium-sulfur batteries. The layered $VS_2$ nanomaterial features Li-ion transport channels, metallic conductivity, and active capacity contribution, all of which provide an ideal platform for the solid-state S/$Li_2S$ redox couple to unlock its high

gravimetric capacity. The $S/VS_2$ hybrid cathode composite was prepared by a facile, low-cost, and low-energy mechanical blending process. The all-solid-state cell using $S/VS_2$ hybrid cathode exhibited sulfur utilization of ~85%, with a coulombic efficiency of close to 100 %. High areal capacity up to 7.8 $mA \cdot h \cdot cm^{-2}$ with an active material loading ($S/VS_2$) as high as 15.5 $mg \cdot cm^{-2}$ was achieved.

In my second project, I reported a $Li_2S/LiVS_2$ core shell composite synthesized from lithium sulfide reacting with metal halide for cathode active materials in all solid-state Li-S battery. Compared with $VS_2$-S composite, $Li_2S/LiVS_2$ core shell composite has an advantage of accommodating the volume change by confining $Li_2S$ in metal sulfide shell during cycling. This approach results better cycle stability and capacity retention in solid-state cell. In this project, both bulk and nanosized $Li_2S$ particles were used for synthesis of core shell composite. With 60 wt% of $Li_2S$ impregnated in the composite, the $Li_2S/LiVS_2$ core shell composite synthesized from nanosized $Li_2S$ yielded an initial capacity of 0.72 $mA \cdot h \cdot cm^{-2}$ with a 75% total utilization over 50 cycles at C/10.

# ACKNOWLEDGEMENTS

I would like to express my sincere gratitude and appreciation to my supervisor Prof. Linda F. Nazar, for her support, and for her guidance and instructions throughout my research project.

I would like to thank my committee members, Prof. Holger Kleinke, Prof. Rodney Smith, and Prof. Anna Klinkova for their help.

I would like to thank all research group members who have supported me in my experiments with generosity and kindness and who have made this experience more enjoyable: Particular thanks to Chun Yuen Kwok, Laidong Zhou, Dr. Zhizhen Zhang, Alireza Mashayekhi, and Ivan Kochetkov.

# TABLE OF CONTENTS

# LIST OF FIGURES

# LIST OF TABLES

# LIST OF ABBREVIATIONS

| | | |
|---|---|---|
| AC | – | Alternating current |
| AB | – | Acetylene black |
| b-$Li_2S$ | – | bulk-$Li_2S$ |
| CE | – | Coulombic efficiency |
| CV | – | Cyclic voltammetry |
| EIS | – | Electrochemical impedance spectroscopy |
| EDX | – | Energy dispersive X-ray analysis |
| GO | – | Graphene oxide |
| Li-ion | – | Lithium-ion |
| Li-S | – | Lithium-sulfur |
| LiPS | – | Lithium polysulfide |
| n-$Li_2S$ | – | nano-$Li_2S$ |
| rGO | – | Reduced graphene oxide |
| SSLSB | – | Solid-state lithium-sulfur battery |
| SSEs | – | Solid-state electrolytes |
| SEM | – | Scanning electron microscopy |
| SEI | – | Solid electrolyte interface |
| THF | – | Tetrahydrofuran |
| TGA | – | Thermal gravimetric analysis |
| XRD | – | X-ray diffraction |

# Chapter 1 Introduction

## 1.1 Overview of rechargeable lithium batteries

With an increasing world population, there is a dramatic increase in energy demands. Currently, global energy supplies predominantly come from fossil fuels. However, these energy sources are unevenly distributed around the globe and exports are controlled by only a handful of countries, which may slow down the global economic development.[1] The extraction of fossil fuels for energy also produces $CO_2$ and other pollutants, which are known causes of severe environmental problems including global warming and air pollution.[2] It is essential to reduce our dependence on fossil fuels and the solution is to discover and develop renewable energies that are profitable and efficient.

Renewable energy from solar, wind, geothermal and nuclear sources are all promising alternatives to fossil fuels. With decades of research already having gone into renewable energy, its energy conversion efficiency should finally match that of fossil fuels soon, which could therefore reduce our dependence on fossil fuels. To utilize alternative energy in practice, wide-scale and portable energy storage devices are required. Rechargeable batteries are good candidates due to having high energy density, a low-cost structure, and high conversion efficiency for delivering energy as electrical energy. Rechargeable lithium-ion batteries have been widely used in laptops, cell phones and other portable electronic devices. Additionally, some companies, such as TESLA and BYD, have commercialized advanced electric vehicles that use rechargeable batteries. The rising demand for more powerful personal electronics and long-range electric vehicles has

encouraged both scientists and engineers to develop advanced high energy density rechargeable batteries.

### 1.1.1 Basic concepts

Lithium-ion rechargeable batteries are secondary batteries and have a certain amount of charge/discharge cycles over their lifespan. They are more efficient and environmental-friendly than primary batteries (single usage, *e.g.* alkaline batteries).[3] An electrochemical cell is composed of two electrodes: a cathode and an anode, which are separated by an electronically insulating and ionic conducting medium called electrolyte. Commonly, a practical Li-ion battery consists in a couple of connected electrochemical cells that work in series and/or in parallel to reach the voltage and current output requirements for a given application.

After connecting two electrodes via an external electric circuit, the difference in chemical potentials between the two active materials during the discharging process gives rise to ion conduction through the electrolyte. The oxidation and reduction half-reactions take place in the anode and cathode, respectively. During the charging process meanwhile, the reactions at the two electrodes are reversed. In order to satisfy the transfer of electrons and ions during the cycling process, both electrodes should be ionically and electronically conductive. The electrolyte is an ionic conductor but also an electric insulator and can be either in a solid or liquid state.

There are several basic electrochemical concepts that are used to characterize an electrochemical cell's performance. The following information will focus on defining an electrode's potential, discharge/charge voltage profile, specific capacity, energy density,

rate capability and cycling performance, which are important factors for understanding the work in this thesis.

The potential (V) of an electrode is related to the redox potential of the reaction occurring at the electrode. The potential difference between cathode and anode is expected to be as large as possible, because output power equals to product of current and potential difference of the two electrodes. At the same time, large potential difference requires suitable electrolytes, which can work properly and avoid decomposition in the electrochemical potential window of the cell.

The discharge/charge voltage profile is a plot of voltage serving as a function of specific capacity during the galvanostatic cycling. Usually, a constant discharge/charge current is applied to the battery in this profile. However, discharge/charge curves showing rate capabilities of cells require varied current density. In a typical discharge/charge voltage profile, intermediary redox reactions and their corresponding voltages are clearly presented. Usually, a plateau in plot represents a two-phase transition reaction while a slope indicates a single-phase reaction. A voltage difference between discharge and charge is an indicator of degree of polarization, which is expected as tiny as possible for reaching maximum of the energy efficiency.

The specific capacity (in mA·h/g) or areal capacity (in mA·h/cm$^2$) is defined by the amount of charge (Q, in mA·h) stored per mass or area of electrode for one full discharge/charge. For most electrode systems, the higher the theoretical specific capacity, the better. In industry, it is common to evaluate batteries in terms of energy density, which is the product of capacity and voltage per mass (W·h/kg) or volume (W·h/L).

The current that passes batteries during discharge/charge is important because it is

related to the power density. In many papers, the concept of "C/n" was used to represent the current density (mA/g) at which the theoretical specific capacity is achieved in n hours upon discharge or charge. The advantage of using higher rate is achieving higher power output. However, the increasing current increases polarization, thus leading to lower specific capacity. Batteries with high-rate capabilities can maintain their capacity and low degree of polarization at high current density.

Cycling life usually refers to the capacity retention of a cell after long-time discharge/charge cycles. In laboratory research, the cycle life of a cell is usually tested by cycling a cell in a galvanostatic mode continuously with a constant current until the capacity decays substantially. In industry, the cycle life is quite important since it directly relates to actual life of applications. The industrial test is more complicated, which usually uses varied rate and rests periodically.

The coulombic efficiency is the ratio of the discharge specific capacity to the charge specific capacity of the same cycle. It can provide an analysis on the stability of a cell after a certain number of cycles.

Among all rechargeable battery types, lithium-based cells have become the most commonly researched due to their high energy densities. Currently, lithium-ion cells occupy a lot of the market which previously belonged to nickel-based batteries.

### 1.1.2 Intercalation and integration electrochemistry

There are two operating mechanisms in a battery's cathode. One is based on intercalation electrochemistry and another is based on integration electrochemistry. In intercalation-based cells, cathodes store/release $Li^+$ ions *via* a topotactic intercalation

process; and in integration-based cells, $Li^+$ ions react with the cathodes' active material in reverse so as to store/release $Li^+$ ions.

In 1980, Goodenough *et al.* proposed $LiCoO_2$ as a cathode active material based on intercalation electrochemistry.[4] The first Li-ion batteries were commercialized by the SONY Corporation using the layered structure of $LiCoO_2$ as the cathode and graphite as the anode, and these still exist in the lithium battery market today. With its higher specific capacity (170 mA·h/g) and better stability due to the presence of $PO_4^{3-}$ tetrahedra in its structure, $LiFePO_4$ also attracted attention. Since $LiFePO_4$ itself is not a good electronic conductor, $LiFePO_4$/C cathodes are usually considered when being applied in industry. Roles for $LiFePO_4$ cathodes are being found in solar-powered lighting systems and backup power due to their low cost, low toxicity, and long-term stability.

Conventional Li-ion batteries have been successfully commercialized and widely applied in daily electronic devices. However, after 40 years of research and practical optimization, these Li-ion batteries established on intercalation-based mechanisms have reached their theoretical capacity limits. In addition, the electrochemical-stability window of most electrolytes does not allow for the cycling of these batteries in a wider voltage range for more energy density. For this reason, conventional Li-ion batteries cannot satisfy the higher energy density required for electric vehicles or other large scale electric devices.[5] To solve this problem, integration-based lithium cells have become potentially viable candidates for the next-generation of batteries. Among them, Li-S batteries with high specific capacity are gaining considerable attentions as energy storage devices. Details on Li-S batteries will be introduced in the next section.

## 1.2 Lithium-sulfur batteries

### 1.2.1 Basic principles

A conventional lithium-sulfur battery consists of sulfur ($S_8$) as its cathode active material and lithium metal as its anode. The cathode and anode are separated by a polymer separator, and the Li-ion transport relies on a supporting electrolyte comprised of a lithium salt dissolved in an ether-based organic electrolyte.[6] In this battery configuration, the cycling operation is typically initiated with a discharge. During discharge (**Figure 1.1a**), two lithium metal atoms are oxidized at the negative electrode to produce two pairs of $Li^+/e^-$. While the produced lithium ions migrate through the electrolyte to the positive electrode, the electrons travel to the positive electrode *via* an external circuit, which thus generates an electrical current. At the positive electrode, sulfur accepts the lithium ions and electrons and is thus reduced to form lithium sulfide ($Li_2S$). During charge, the lithium

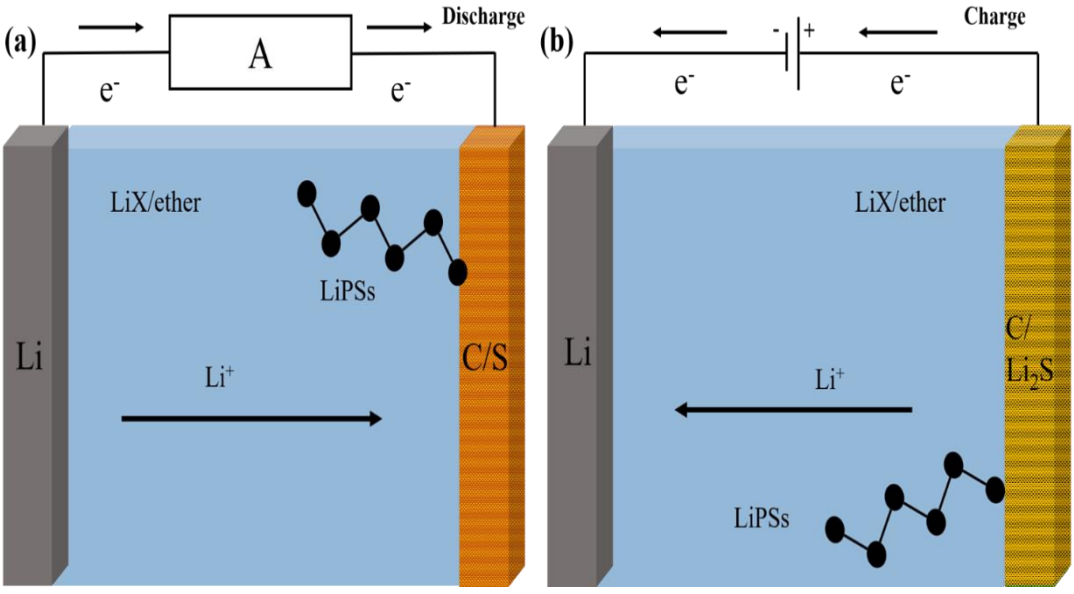


**Figure 1.1** Schematic diagram of the discharge (a) and charge (b) mechanism in a Li-S battery

sulfide is oxidized back to sulfur as the lithium ions are deposited on the lithium anode (**Figure 1.1b**). The reversible electrochemical reaction of $16Li^+ + S_8 + 16e^- \leftrightarrows 8Li_2S$ exhibits an average potential of 2.15 V *vs.* $Li/Li^+$, affords a high specific capacity of 1675 $mA \cdot h \cdot g^{-1}$, and an energy density of 2500 $W \cdot h \cdot kg^{-1}$, with respect to the sulfur cathode.[7]

## 1.2.2 Challenges posed by lithium-sulfur batteries

Li-S batteries exhibit many advanced features over conventional lithium-ion batteries (LIBs), including higher energy density and lower material cost. While Li-S batteries show great potential to become the next generation of energy storage, some challenges remain to be resolved before commercialization. These challenges include large volume changes during cycling, lithium dendrite formation, lithium polysulfide shuttling effect, and the insulating natures of sulfur and lithium sulfide.[7]

**Physical properties of $S_8$/$Li_2S$.** In the cathode of a Li-S cell, the sulfur receives electrons from the external circuit and reacts with the Li+ ions transferred from the lithium anode through the electrolyte. The cathode should therefore have the ability to transfer enough electrons and Li-ions to the active materials. However, both sulfur (electronic conductivity $\approx 10^{-30}$ $S \cdot cm^{-1}$) and its discharge product $Li_2S$ (electronic conductivity $\approx 10^{-14}$ $S \cdot cm^{-1}$) are electronically and ionically insulated at room temperature.[8] These insulating properties lead to poor kinetics and greatly constrain the utilization of the active materials. The poor electrochemical utilization of the active material then results in large overpotentials and low energy densities. To improve its electrical conductivity, carbon conductive additives are often introduced into the sulfur cathode. However, due to carbon's low density, this decreases the overall volumetric energy density of the battery.

Another issue is volumetric expansion/contraction during the continuous cycling process. There is a solid-liquid-solid multiple-phase transition from sulfur to $Li_2S$ and *vice-versa*, which causes an 80% volume change due to density differences ($\rho_s$ = 2.07 g·cm$^{-3}$ *vs.* $\rho_{Li_2S}$ = 1.66 g·cm$^{-3}$).[7] This large volume change can deteriorate cathode structure and integrity, resulting in a break in the electronic pathway at the cathode and a decrease in capacity over long-term cycling.

**Lithium anode.** In Li-S devices, lithium metal is used as the anode. However, lithium metal can readily react with water or oxygen.[9] For safety reasons, lithium metal must therefore be completely isolated from air, which limits the commercialization of Li-S cells. In addition, dendrite growth on the lithium metal in Li-S batteries is another issue that not only results in poor columbic efficiency but also poses a major safety hazard. The mossy electrodeposition of lithium ions on the lithium anode during the charge process results in dendritic structures instead of a uniform and smooth surface. These dendritic structures can break the stable solid-electrolyte interface (SEI) at the anode – typically formed when lithium metal is oxidized by the surrounding electrolyte molecules –, and thereby lead to higher electrolyte consumption due to the need to reform new SEI layers. Continuous dendrite growth will eventually penetrate the separator and reach the cathode, resulting in the short-circuiting of the cell or even an explosion. For these reasons, practical application of lithium metal is limited and novel anode materials with high energy density are needed to match with sulfur cathodes.[9]

**Polysulfides shuttle.** During cycling, sulfur electrochemically undergoes a complicated morphological and compositional change by forming lithium polysulfides ($Li_2S_x$: $1 < x \leq 8$) as intermediate species. The high-order lithium polysulfides ($Li_2S_x$: $4 <$

x ≤ 8) are soluble in the ether-based electrolyte. **Figure 1.2** shows the polysulfide shuttle effect. Upon discharge, these dissolved lithium polysulfides migrate out from the sulfur cathode host and diffuse through the porous polymeric separator to the Li metal anode as a result of a chemical potential and concentration gradient between the two electrodes. The leached lithium polysulfides are immediately reduced on the Li metal surface to form an insulating and insoluble $Li_2S/Li_2S_2$ layer. Upon charge, $Li_2S$ is converted into metallic Li and sulfur, while the redox shuttling of soluble lithium polysulfides leads to the precipitation of $Li_2S$ at the exterior cathode surface. This undesired and uncontrolled polysulfide migration leads to a continuous loss of active materials and severe lithium metal degradation. This process – the polysulfide shuttle effect – is also the origin of low coulombic efficiency, low-capacity retention, and serious self-discharge phenomena that is observed in liquid lithium–sulfur batteries.[10,11]

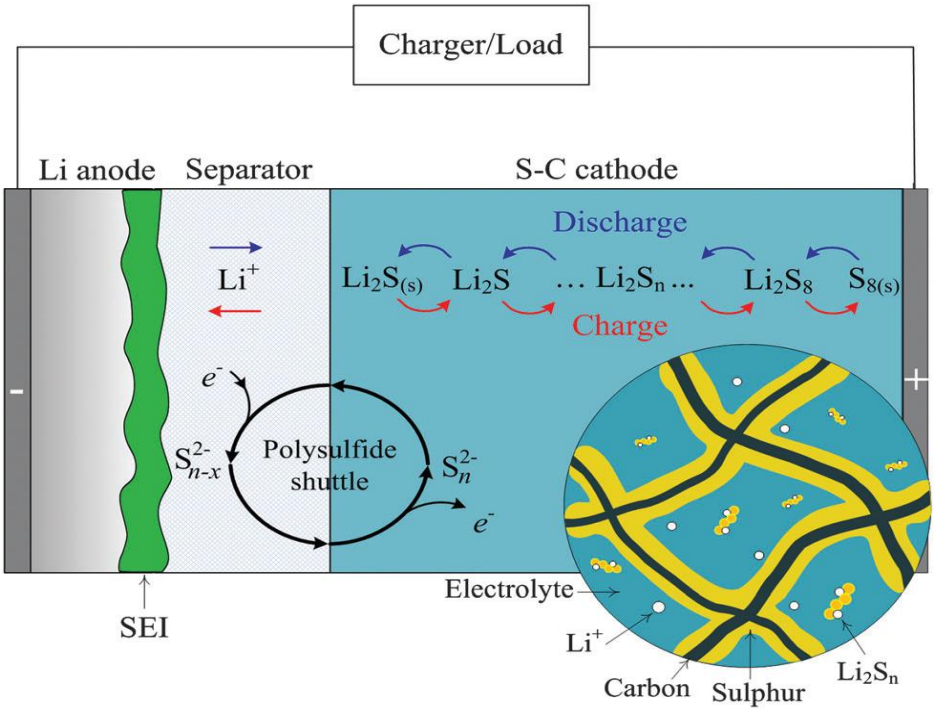


**Figure 1.2** The schematic diagram of the lithium polysulfide shuttle effect, reproduced with permission from reference 11.

### 1.2.3 Investigation on cathode of conventional Li-S batteries

After decades of research, conventional lithium-sulfur cells still suffered from the problems of low sulfur utilization and diffusion of lithium polysulfides. This all changed in 2009 with a major breakthrough that used an ordered mesoporous carbon network (CMK-3) as a cathode host material.[12] Inspired by this work, an increasing number of designs have been developed, and numerous new sulfur-based nanocomposites have been employed as cathode materials. In this section, nanostructured carbonaceous materials, doped carbon and other nanostructured polar inorganic compounds are briefly introduced.

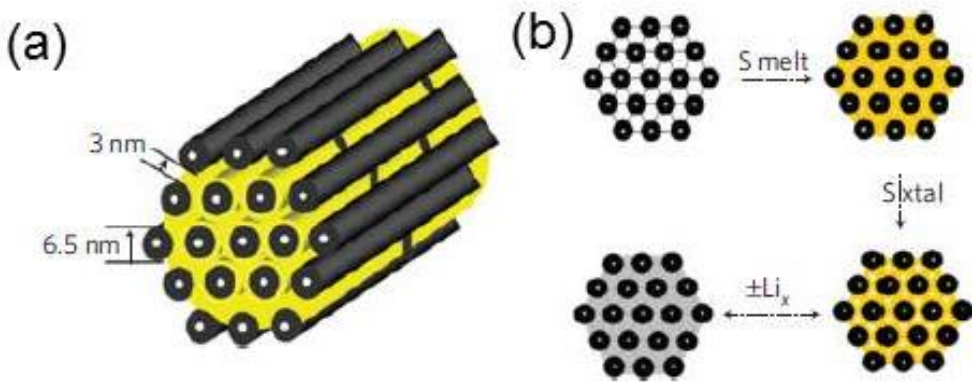


**Figure 1.3** (a) Structure of S/CMK-3 composite. (b) Schematic diagram of sulfur melt diffusion and how sulfur (yellow) turns into $Li_2S$ (grey) upon discharge, reproduced with permission from reference 12.

Due to the good electronic conductivity of carbonaceous materials, they are frequently used to host sulfur by forming C/S composite cathode materials. These carbonaceous materials include mesoporous carbon, microporous carbon, hierarchical porous carbon, carbon black, hollow carbon spheres, carbon nanotubes (CNTs), and carbon nanofibers (CNFs).[13] Although these host materials significantly improve sulfur utilization

for practical Li-S cells, the nonpolar nature of these carbonaceous materials can only act as a physical barrier for the polar polysulfide. Upon long-term cycling, the LiPSs still eventually migrate out of the cathode host. Nonetheless, the initial work of the CMK-3 material (**Fig. 1.3 a-b**) still demonstrates a high initial specific capacity of 1320 $mA \cdot h \cdot g^{-1}$, approaching 80% sulfur utilization.[13]

Since nonpolar carbon materials have difficulty in effectively anchoring lithium polysulfides, doped carbon with tunable polar sites and effective electron pathways has been proposed in order to provide more efficient chemical binding sites.[14] These doped carbon host materials contribute conductive scaffolds, and their functional groups offer additional chemical anchoring sites. Some of these early works are exemplified by graphene-polymer composites, graphene oxides and N-doped carbon materials. For example, graphene sheet-wrapped sulfur particles were reported as cathode hosts in 2011.[15] This poly (ethylene glycol) (PEG)/graphene composite coating helped accommodate the sulfur active material's volume expansion during cycling and prevented the polysulfide from diffusing out of the cathode, thereby resulting in a stable capacity of 600 $mA \cdot h \cdot g^{-1}$ for more than 100 cycles. Graphene oxide was also proposed by Zhang *et al.* as a host material.[16] A nanosized uniform sulfur coating on graphene oxide sheets was obtained by chemical reaction-deposition and a subsequent low-temperature thermal process. The strong interactions between graphene oxide and sulfur or polysulfides enables Li-S cells with a high reversible capacity up to 1400 $mA \cdot h \cdot g^{-1}$, and stable cycling for more than 50 deep cycles at 0.1C to be fabricated.

In addition to carbonaceous materials, nanostructured inorganic compounds, such as transitional-metal oxides, sulfides, and carbides have also been reported as polar sulfur

host materials in recent years.[17] These compounds are much more efficient at adsorbing polysulfides than nonpolar carbon materials, thereby rendering Li-S cells with excellent capacity retentions. This is attributed to the large number of anchoring sites for polysulfides in these high surface area materials. Furthermore, these inorganic host materials may improve the kinetics during the electrochemical conversion of lithium polysulfides to lithium sulfides, and *vice-versa*. In addition, when transitional-metal sulfides or oxides are applied in cathodes, the rate capability and areal sulfur loading of Li-S batteries can be enhanced.[17]

Some metal oxides contain oxygen as $O^{2-}$ and have a strong polar surface, which is inherently hydrophilic and used in liquid cells. They tend to be insoluble in most organic solvents and are mainly used as additives/modifiers for existing nanostructured C/S cathodes. For instance, in 2001 Gorkovenko *et al*. patented vanadium oxides, silicates, and aluminum oxides for applications in suppressing polysulfide migration in sulfur cathodes.[18] However, their polysulfide adsorbabilities were limited due to the adsorbing agents' large particle sizes. In consideration of the effect that size has, Song *et al.* added nanosized manganese nickel oxide particles (30-50 nm) into the sulfur cathodes, thus achieving where excellent cell performance with a capacity retention of 85% for 50 cycles.[19] From these results then, small particle sizes, porous structures, and high surface areas have all been identified as being important criteria for these adsorbing agents. Manganese nickel oxide, and titania are both representative metal oxides with effective polysulfide adsorbing sites.[20,21] The fact that these materials only contribute a small fraction (*e.g.,* 3.6 wt. % for $TiO_2$ and 15 -20 wt. % for $Mg_{0.6}Ni_{0.4}O$) to the overall cathode weight, and yet can result in

major improvements in capacity retention, suggesting that they are practical additives for the cathode.

With increasingly facile synthesis methods being reported for two-dimensional dichalcogenides in recent years, these materials have been explored as being potential sulfur host materials in liquid Li-S batteries. Metal sulfides, such as $MoS_2$, $VS_2$, and $TiS_2$ have many advantages over their oxide cousins, such as having stronger affinities with sulfur-containing species.[22] More specifically, in 2017 Liu *et al.* used an organic electrolyte to fabricate $VS_2$/reduced graphene oxide nanosheets as a sulfur host, as shown in **Figure 1.4**.[23] In this rGO-$VS_2$ hybrids material, 2D conductive and polar $VS_2$ is interlayered within a graphene framework, which suppresses polysulfide shuttling, facilitates the charge transport, and accommodates volume expansion throughout the synergistic effects of structural confinement and chemical anchoring. With these advantageous features, this sulfur cathode (rGO–$VS_2$/S) can deliver a capacity of 950 and 800 $mA{\cdot}h{\cdot}g^{-1}$ at 1 and 2 C, respectively. Moreover, after 300 cycles at 5 C, the cathode still

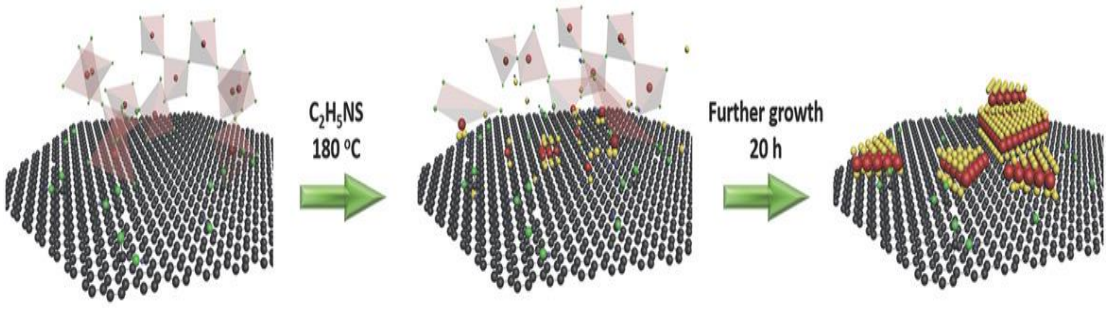


**Figure 1.4** Illustration of the *in situ* self-assembly of vanadium disulfide on reduced graphene oxide to form rGO-$VS_2$ hybrids, reproduced with permission from reference 23.

maintains a capacity of 532 $mA{\cdot}h{\cdot}g^{-1}$, which shows an impressive cycling stability.

From the above examples, it is clear that nonpolar nanostructured carbonaceous materials, doped carbon and other nanostructured polar inorganic compounds can trap polysulfide by using physical or chemical adsorption. However, these methods still do not completely solve the polysulfide shuttling problem. Fortunately, solid-state cells can offer a solution to this problem, and this is the reason that this thesis focuses on solid-state Li-S batteries.

Apart from the cathode side, there are many approaches that focus on other aspects with an intent to extend cycle life, including using lithium polysulfides-insoluble electrolytes, modified separators, anode coating, and interlayering between cathode and separator.[24] However, these will not be introduced in detail in this paper.

## 1.3 Solid-state lithium sulfur battery

### 1.3.1 Basic concepts

The configuration of solid-state cells is similar to that of a conventional liquid cell. The only difference is that solid-state cells employ a solid-state electrolyte instead of a liquid one between cathode and anode. This substitution removes the risk that the flammable organic liquid will catch fire, while the solid-solid interfacial interaction between the electrode and electrolyte (separator) materials often leads to a high resistance. Usually, external pressure is needed to enable intimate contact between them. In addition, the composite cathode requires good ionic and electronic conductivity to support the redox reactions. Therefore, the cathodes in solid cells are typically composed of active material, with an ionic conductor (solid electrolyte) and an electronic conductor, which thus differs from a conventional liquid cell.[25,26]

Compared with the conventional liquid lithium-ion batteries on the market, all-solid-state batteries have some advantages when applied for large energy storage, such as in electric vehicles that require high energy density and better safety. First, a solid battery's volume can easily be reduced, and thus relatively larger energy outputs can be achieved. Second, due to the removal of liquid flammable electrolytes, solid cells are not as sensitive to shocks, leakages, and extreme temperatures as liquid cells. However, lithium solid-state batteries have their own drawbacks, such as having higher ionic resistance than liquid cells. In addition, solid-state electrolytes are more expensive to fabricate.[27]

Solid-state lithium sulfur battery (SSLSB) refers to a solid-state cell that employs S/$Li_2S$ as the active materials in cathode. It has been proposed as a promising alternative to the conventional liquid sulfur battery due to its good electrochemical performance, life stability, safety, and potential application in the field of electric vehicles. There are two different SSEs that have been used in solid-state Li-S batteries. One type is organic solid polymer electrolytes (*i.e.*, lithium salts (*e.g.*, $LiClO_4$, $LiPF_6$, $LiN(SO_2CF_3)_2$, etc.) dissolved in a high molecular weight polymer host such as polyethylene oxide (PEO)).[28] Liquid electrolytes or polymer electrolytes exist when applying organic solid polymer electrolytes, and these present a typical discharge-charge profile similar to that of the Li-S cells using ether-based liquid electrolytes. The other type is inorganic glassy/ceramic electrolytes, which mainly include sulfides (*e.g.*, glass/glass–ceramic $Li_2S$-$P_2S_5$)[29] and oxides (*e.g.*, garnet-type $Li_7La_3Zr_2O_{12}$).[30] When applying inorganic electrolytes, the sulfur redox chemistry in solid-state Li-S batteries is different from that in liquid electrolyte Li-S cell. The lithium-sulfur system's equilibrium phase was investigated and it was found that in addition to sulfur, only one $Li_2S$ solid compound was observed, indicating therefore that only $Li_2S$ was

formed during the solid-state reaction.[31] The *ex situ* S *K*-edge X-ray absorption fine structure measurements for the all-solid-state lithium battery with $Li_2S$-carbon composite positive electrode further confirmed the direct electrochemical reaction from sulfur to $Li_2S$.[32] This solid-solid reaction is common in sulfide-based SSE systems. In this thesis, the solid electrolytes used in solid-state Li-S batteries are inorganic glassy/ceramics electrolytes, especially sulfide-based electrolytes.

### 1.3.2 Solid-state electrolytes

Solid electrolytes (SEs) are essential components that act as both a separator and a $Li^+$ conductor in the ASSLSBs. Since electrolytes have a large influence on battery performance, these should be chosen carefully when designing a reasonable and practical battery.[33] The development and classification, ionic conductivity, and functions of various SEs have been discussed in a large number of reviews. In this thesis, two main inorganic solid-state electrolytes used in solid-state Li-S batteries will be briefly introduced in this section.

Sulfide-based SSEs exhibit relatively high ionic conductivities and are widely used in solid-state lithium sulfur batteries. Common sulfide-based electrolytes used in solid-state Li-S batteries include glass/glass-ceramic $Li_2S$-$P_2S_5$, $Li_{10}MP_2S_{12}$ (M = Ge, Sn, Si), and argyrodites $Li_6PS_5X$ (X = Cl, Br, I). Glass/glass-ceramic $Li_2S$-$P_2S_5$ is an important member of the sulfide solid electrolyte family, and exhibits ionic conductivities of over $10^{-4}$ S $cm^{-1}$ at RT.[33] As a very promising electrolyte candidate for solid-state batteries, it offers advantages like low cost, reasonable ionic conductivity and acceptable electrochemical windows vs. $Li/Li^+$. Among the various compositions, $Li_3PS_4$ and $Li_7P_3S_{11}$ are two

representatives which have been widely used as solid-state electrolytes in Li-S work. $Li_3PS_4$, which was used in one of my projects, has been extensively studied due to its facile synthesis, and good compatibility with lithium metal. However, $Li_3PS_4$ in the cathode composite functions not only as an ionic conduction path but also as an active material.[34] Hakari *et al*. investigated the structural and electronic-state changes in $Li_3PS_4$ during the Li deinsertion-insertion processes.[35]The sulfide ions in $Li_3PS_4$ undergoes electrochemical oxidation on charge, which contributed additional capacity. In cycling, covalent bonds between the P atoms and S-S bonds are maintained while the S-S bonds between $PS_4$ units associate and dissociate. The electrochemical window of $Li_3PS_4$ calculated by using DFT indicates that oxidation reaction of $Li_3PS_4$ is the conversion of $Li_3PS_4$ to S and $P_2S_5$.[36] However, this oxidation reaction was not proved in experiment. Based on XPS spectroscopy data from work of Hakari *et al.*,[35] the most likely oxidation structure is considered to result from the formation of S-S bonds between the $PS_4$ units. On the other hand, $Li_7P_3S_{11}$ also attracts a lot of interest as by hot-pressing at room temperature it can demonstrate a high ionic conductivity of $1.7 \times 10^{-2}$ S $cm^{-1}$.[37] To further improve the ionic conductivity of the glass/glass-ceramic $Li_2S$-$P_2S_5$ system, ternary sulfide solid electrolytes with higher conductivities are proposed. Ternary $Li_2S$-$M_xS_y$-$P_2S_5$(M = Ge, Sn, Si) systems can be synthesized by incorporating the third component, such as $GeS_2$, into the binary sulfide solid electrolytes to substitute the $P_2S_5$.[38] This incorporation creates lithium vacancies by partial aliovalent substitution, thus increasing the ionic conductivity of the $Li_{10}MP_2S_{12}$ (M = Ge, Sn, Si) family. As a representative of the $Li_{10}MP_2S_{12}$ family, $Li_{10}GeP_2S_{12}$ can exhibit an ionic conductivity as high as $10^{-2}$ S $cm^{-1}$ at room temperature, which even competes with that from liquid electrolytes. However, the $Li_{10}MP_2S_{12}$ (M =

Ge, Sn, Si) families highly reactive to lithium metal, which means a need for extra anode protection. Another highly ionic solid-state electrolyte family is the $Li_6PS_5X$ (X = Cl, Br, I)) family, which can exhibit an ionic conductivity close to $10^{-2}$ S $cm^{-1}$. The addition of halides can increase this system's conductivity since halogen anions partially substitute sulfur and stabilize the original crystal structure. Our group reported a new halide-rich solid solution phase in the argyrodite $Li_6PS_5Cl$ family, $Li_{5.5}PS_{4.5}Cl_{1.5}$, which exhibited a cold-pressed conductivity of ~9.4 mS $cm^{-1}$ at 298 K.[39] The $Li_{5.5}PS_{4.5}Cl_{1.5}$ has a better ionic conductivity than regular $Li_6PS_5Cl$ (~5 mS $cm^{-1}$) since interactions between the mobile Li-ions and surrounding framework anions are weakened by substitution of divalent $S^{2-}$ for monovalent $Cl^-$, causing higher Li-ion diffusivity. The $Li_{5.5}PS_{4.5}Cl_{1.5}$ was utilized in one of my research projects as solid ionic conductors. Though the $Li_6PS_5X$ (X = Cl, Br, I)) family has good chemical stability with the lithium anode, it is electrochemically instable with lithium metal, meaning that an extra layer of anode protection is necessary. Though most sulfide SSEs have excellent ionic conductivity, their narrow electrochemical stability windows and chemical instability when in an air environment pose challenges for the development of a solid-state Li-S battery.

Common oxide-based electrolytes include garnet-type $Li_7La_3Zr_2O_{12}$, NASICON-type $Li_{1+x}Al_xTi_{2-x}(PO_4)_3$ (LATP) and $Li_{1+x}Al_xGe_{2-x}(PO_4)_3$ (LAGP), and perovskites-type $Li_{3x}La_{(2/3)-x}TiO_3$ (LLTO). Though oxide solid electrolytes have ionic conductivities in a range of $10^{-4}$–$10^{-2}$ S $cm^{-1}$ under room temperature, they are not widely used as single components of SE due to the large interfacial resistance between oxide-based electrolytes and electrodes in solid-state Li-S batteries.[40] In addition to serving as an SE layer, oxide-based SSEs can couple with polymer-based SSEs, liquid electrolytes, or ionic liquids to

reduce interfacial resistance. However, coupling with other electrolytes leads to a hybrid SSE system, which complicates the battery system. The hybrid SSE system will not be discussed in this thesis.

### 1.3.3 Investigation on cathode of solid-state lithium sulfur batteries

Compared with conventional liquid Li-S batteries, the different reaction mechanisms in SSLSBs require more complex and innovative cathode designs. Traditional designs like confining sulfur in porous carbon matrixes will no longer work due to poor contact between SSEs and sulfur limiting the $Li^+$ transference. This section will introduce some approaches to the cathode design of solid-state Li-S batteries.

In recent years, many studies have been carried out on all-solid-state Li-S batteries with sulfide-based electrolytes, where the solid electrolyte is mixed with carbon-sulfur composite material through extensive ball-milling. For instance, Tatsumisago *et al.*[41] reported on a solid-state Li-S battery with $Li_2S$-$P_2S_5$ glass-ceramic electrolytes. The cathode showed that the different mixing methods used to prepare the composite have a large influence on cell performance. They showed that cathode prepared by ball-milling delivered a significantly higher capacity compared with that prepared by mortar grinding. This increased capacity is attributed to the amorphization of sulfur and the reduction in the mixture's particle size by the milling of sulfur, acetylene black and the $Li_2S$-$P_2S_5$ glass-ceramic electrolyte. The solid-state cell with milling composite cathode exhibited a reversible capacity of 850 $mA{\cdot}h{\cdot}g^{-1}$ for 200 cycles under 1.3 mA $cm^{-2}$ at 25 °C. In addition, their work also shows that the intimate contact between cathode components can be improved through mechanical ball-milling.

In another case, Nagada *et al.*[42] reported on an all-solid-state lithium-sulfur battery with composite cathode using a high phosphorus-to-sulfur (P/S) ratio solid electrolyte. In this work, the activation energy was claimed to be almost independent of the active materials' loading weight, which suggests that sulfur reactivity, with relation to P/S ratio, has a significantly larger influence on battery performance than the ionic and electric conductivities do. The cathode is assembled using a sulfur-AC composite, with $Li_{1.5}PS_{3.3}$ ($60Li_2S$-$40P_2S_5$) serving as a high P/S ratio SE. The solid-state cell using the above cathode, $Li_{10}GeP_2S_{12}$ as the SE layer, and Li-In alloy as the anode displayed a capacity of up to 1850 $mA{\cdot}h{\cdot}g^{-1}$ at a loading of 1.5 mg $cm^{-2}$, which is even higher than sulfur's theoretical capacity (1675 $mA{\cdot}h{\cdot}g^{-1}$). The additional capacity was contributed by the decomposition of electrolytes. A remarkable cycle life beyond 1000 cycles when under high working currents of 1.3 mA $cm^{-2}$ was also achieved.

Sun *et al*. have reported on an all-solid-state Li-$SeS_x$ battery, where the ionic conductivity of the S ring was improved by replacing the sulfur atoms in the $S_8$ ring with Se atoms.[43] In their work, Se was co-melted with S to form an $SeS_x$ (x=3, 2, 1, 0.33) solid solution. $SeS_x$ is a ring similar to the $S_8$ ring, in which some S atoms are substituted by Se

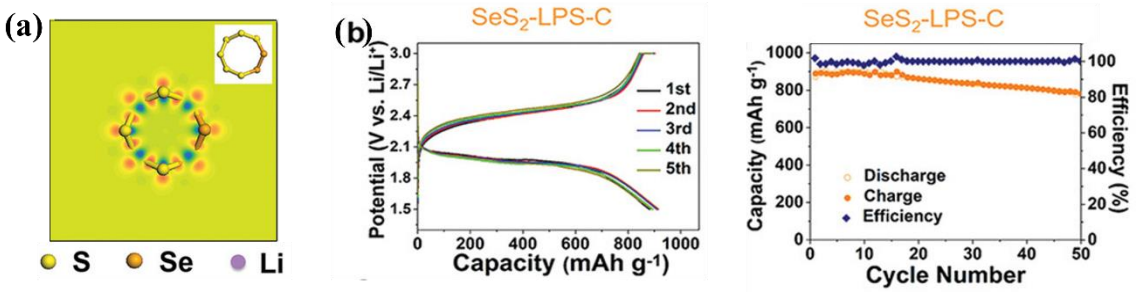


**Figure 1.5** (a) Schematic illustration of electron densities of $Se_2S_6$ rings. (b) Discharge-charge curves of cells with $SeS_2$-LPS-C cathode at 25 °C, reproduced with permission from reference 43.

atoms (**Figure 1.5 a**), thereby resulting in better ionic conductivity. The ionic conductivities of $SeS_2$-$Li_3PS_4$ composites reached $10^{-6}$ S·cm$^{-1}$ at 25 °C, which is higher than that of S-$Li_3PS_4$ under the same conditions. The $SeS_2$-$Li_3PS_4$-C cathode was prepared by ball-milling $SeS_2$, $Li_3PS_4$ and acetylene black at a weight ratio of 2:2:1 for 4h, which exhibited (**Figure 1.5 b**) a capacity of over 1100 mA·h·g$^{-1}$ (98.5% of its theoretical capacity) at 50 mA·g$^{-1}$ and maintained good stability for 50 cycles. In addition, the $SeS_2$ high-loading cell can reached 12.6 mA·h·cm$^{-2}$ at a loading of 15.3 mg·cm$^{-2}$ when a current density of 50 mA·g$^{-1}$ was applied at 60°C.

Lithium sulfide ($Li_2S$) can deliver an acceptable theoretical capacity of 1166 mA·h·g$^{-1}$, meaning that it is a promising cathode material. As a discharging product of sulfur, $Li_2S$ leads to volume reduction when transforming into sulfur, thereby benefiting battery stability. However, its electronically and ionically insulating nature and high sensitivity to air pose challenges when it is used as an active material. Many attempts have been made during recent years to address these issues. The intimate contact among cathode components, and the smaller particle size of the active materials are important for the improvement in the capacity and performance rate of the $Li_2S$ cathode. For instance, Nagao *et al.*[44] prepared cathode composite materials through two different methods: $Li_2S$, acetylene black (AB), and $80Li_2S·20P_2S_5$ were mixed by mortar grinding and ball-milling. The milling cathode composites presented the best performance among different cathodes, since cathode components came into intimate contact. The particle size of both $Li_2S$ particles and $Li_2S$-based electrodes was reduced by ball-milling, which ultimately increased the capacity of the cathode. Their $Li_2S$-AB/$80Li_2S·20P_2S_5$/Li-In solid-state cells with milling cathode materials exhibited a reversible capacity of 800 mA·h·g$^{-1}$capacity at

0.064 mA $cm^{-2}$.

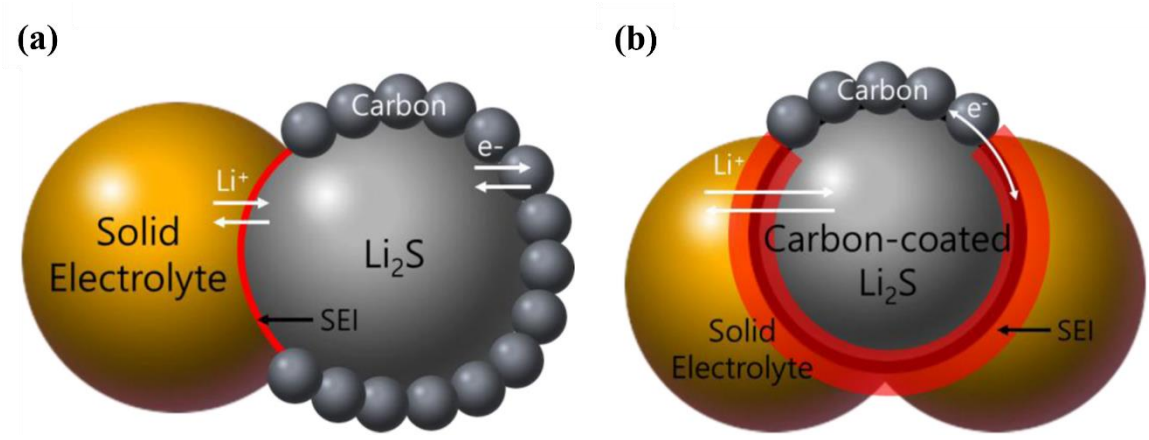


**Figure 1.6** Schematic illustration of the lithium ion and electron transfer in (a) bare $Li_2S$ and (b) carbon-coated $Li_2S$ containing an all-solid-state lithium-sulfur battery, reproduced with permission from reference 45.

In addition, to improve the electronic conductivity of $Li_2S$ composite, Shin *et al.* coated $Li_2S$ with carbon.[45] **Figure 1.6** shows how lithium ion and electron transfer in bare $Li_2S$ and carbon-coated $Li_2S$ containing solid-state cell. The carbon coating used on the $Li_2S$ particles came from a carbonization of polyacrylonitrile at 700 °C. The electronic conductivity of carbon-coated $Li_2S$ increased to $2.39 \times 10^{-2}$ S $cm^{-1}$ (41.89 Ω $cm^{-1}$), which is much higher than that of bare $Li_2S$, which corresponds to $9.21 \times 10^{-9}$ S·$cm^{-1}$. By the 10th cycle, the carbon-coated $Li_2S$ cathode exhibited a capacity of 730 mA·h·$g^{-1}$, in which mass is based on carbon-coated $Li_2S$. This work also reveals the possibility of reducing the total electronic additives ratio in the composite cathode.

Apart from alleviating the electronically insulating properties of $Li_2S$, Xu *et al.* attempted to improve the energy density of most bulk-type all-solid-state Li-S batteries by reducing electrolyte thickness.[46] In their work, a cathode-supported all-solid-state Li-S battery with a thin solid electrolyte layer was reported. At the beginning, a stainless steel

(SS)-supported $Li_2S$ cathode was built, followed by a ~100 μm-thick $Li_3PS_4$ solid electrolyte, with a nonwoven Kevlar scaffold integrated as its mechanical support. **Figure 1.7** showed fabrication process of cell, which is different from traditional electrolyte-supported cells that first build an electrolyte layer and then build electrode layers on both

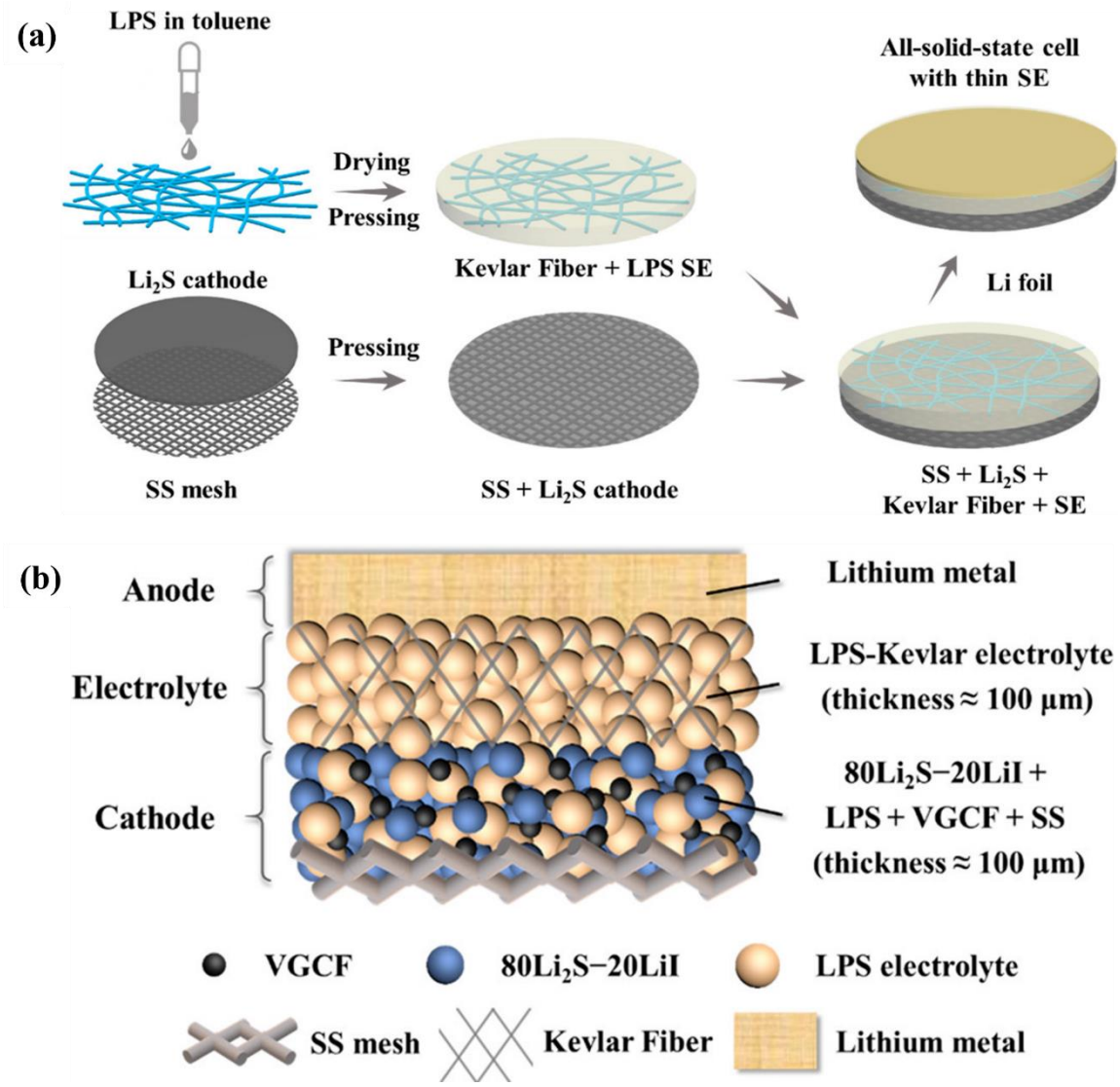


**Figure 1.7** (a) Fabrication of the cathode-supported all-solid-state cell with a thin sulfide electrolyte. (b) Design of the cathode-supported high cell energy all-solid-state Li-$Li_2S$ cell, reproduced with permission from reference 46.

sides. The cell with a $Li_2S$ loading of 2.54 $mg \cdot cm^{-2}$ provided an initial capacity of 949.9 $mA \cdot h \cdot g^{-1}$ at 0.05 C under room temperature. When applying higher active material loading, the areal capacity and energy density of the cell were higher. If the loading of $Li_2S$ increases to 7.64 $mg \cdot cm^{-2}$, the cell can provide a high areal capacity of 6.97 $mA \cdot h \cdot cm^{-2}$, and a high energy density of 370.6 $Wh \cdot kg^{-1}$ at the cell level. However, after 20 cycles, the high-loading cell's capacity decreased rapidly to approximately one-third, which indicates instability in the cell. Though the energy density was not high if the weight of the SS mesh current collector is included in the calculation, this work still inspires an improvement of the energy density of the solid-state Li-S cell.

In short, the above solid-state sulfur cathode designs show that maintaining a good balance between electronic and ionic conductivities, and having intimate contact between the cathode components are essential for achieving good battery cycling performance. Some transitional metal sulfides possess both electronic and ionic conductivities, which may indicate good potential to serve as host materials in solid-state sulfur cathode. My projects concern the application of transitional metal sulfides in solid-state Li-S batteries, which will be introduced in the following sections.

## 1.4 Thesis motivation

The concept of using elemental sulfur as a positive electrode material for liquid electrolyte Li-S cells was first introduced by Helbert and Ulam in 1962, and the first invention of a liquid electrolyte Li-S battery was presented in the late 1960s.[47] During the early stages, researchers focused on improving the utilization of sulfur through dealing with its insulating nature. However, in the 1980s they were faced with a more serious irreversible

polysulfide shuttle problem. It was proposed that the introduction of mesoporous carbon carbonaceous materials (*e.g.* porous carbon, graphene and polymeric materials) as the sulfur host could be a solution to deal with polysulfide shuttling *via* physical confinement and/or chemical interactions. Another solution is the use of inorganic solid electrolytes by all-solid-state Li-S batteries, which in theory completely eliminates the polysulfides. In recent years, a lot of effort has been put into investigating the solid-state Li-S batteries due to their higher energy density, higher capacity retention, and better safety. Therefore, developing a practical solid-state cell system is a promising concept. It is also worth noting that the real sulfur conversion mechanism in solid-state is still under debate and more work is needed to determine how orthorhombic sulfur transforms into cubic lithium sulfide.

## 1.5 Scope of this thesis

This thesis will be focused on new sulfur host materials to effectively improve battery performance of solid-state Li-S cells. ***Chapter 1*** gives a general introduction on the demand for energy storage devices and pertinent research that have been undertaken on both conventional Li-S batteries and solid-state Li-S batteries in the past. ***Chapter 2*** describes the characterization methods and techniques used in this thesis. ***Chapter 3*** examines a nanosheet vanadium disulfide as a sulfur host material and the improved electrochemical performances. ***Chapter 4*** introduces the $Li_2S/VS_2$ core shell composite working as cathode active materials.

# Chapter 2 Characterization methods and techniques

## 2.1 Materials characterization

### 2.1.1 Powder X-ray diffraction

To analyze structure and identify phase composition of crystalline materials, X-ray powder diffraction (XRD) is an ideal analytical technique. When Wilhelm Röntgen discovered X-rays in 1895, physicists were uncertain about nature of X-rays. X-ray was not confirmed as electromagnetic wave until observation of X-ray diffraction in 1912. The year after, Sir William Bragg discovered the law that relates the wavelength of X-ray to the diffraction angle and the lattice spacing in a crystal structure, also known as Bragg's law.

$$n\lambda = 2\,d\sin\theta$$

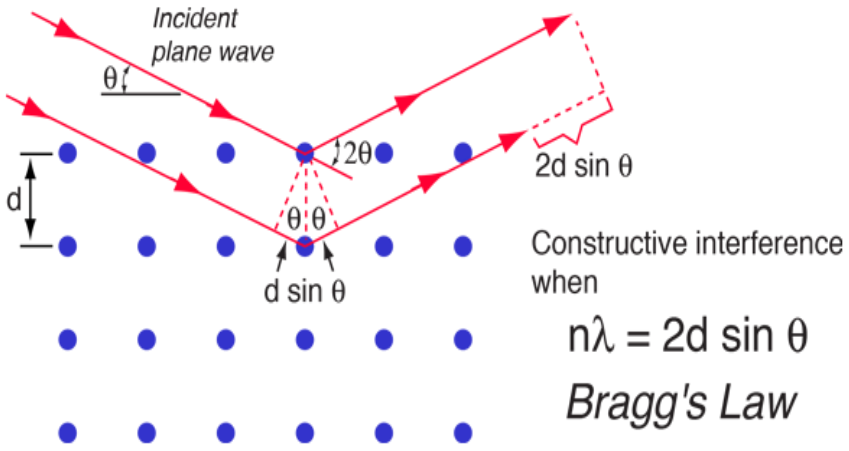


**Figure 2.1** Schematic illustration of Bragg's law, reproduced with permission from reference 48.

Where λ is the wavelength of incident X-ray beams, θ represents the angle between

incident beam and parallel planes, and d is the distance between parallel lattice planes. **Figure 2.1**[48] further describes how Bragg's law is applied in crystallography. In a crystal structure, parallel X-ray beams are diffracted by parallel lattice planes that maintain a distance of d with each other. Bragg's law is satisfied if two X-ray beams interfere constructively with each other. In that case, 2d sin θ is equal to a multiple (n) of the wavelength (λ). Bragg's law is applicable to powder XRD. Every crystal orientation reflects diffraction corresponding to each d spacing, thus giving the information about the structure of material. A diffracted pattern is generated by sending X-ray to the sample while rotating the sample stage with respective to incident beam. As every compound have its unique structure, thus having its unique XRD pattern. By comparing with a comprehensive database, the crystal structure of a sample can be determined.

The X-ray powder diffraction is usually conducted on an instrument referred to an X-ray diffractometer that scans the sample over a range of 2θ and measure the intensity of diffracted X-ray as a function of the angle. The X-ray diffractometer used in this thesis was a PANalytical Empyrean instrument outfitted with a PIXcel two-dimensional detector operating at 45 kV/40mA, using Cu-Kα radiation (λ = 1.5405Å). Air-sensitive samples were measured on a zero-background silicon holder using a protective Kapton film sealed with vacuum grease.

### 2.1.2 Scanning electron microscopy and energy dispersive X-ray spectroscopy

Scanning electron microscopy (SEM) is a useful technique to investigate morphology and topography of solid samples. In a common SEM instrument, the sample surface is

scanned by a focused beam of electrons, producing secondary electrons and characteristic X-rays, which are collected by their respective detectors and transformed into various signals. Secondary electrons are emitted from interactions between incident beam and surface of sample, providing information on the specimen topography. Characteristic X-rays are emitted when outer-shell electrons fill vacancies in the inner shell, in which the inner-shell electrons of sample atoms are removed by incident beam. These characteristic X-rays are detected by energy X-ray spectroscopy (EDX), which can provide an element distribution mapping of the sample area. SEM and EDX measurements in this thesis were performed on a Zeiss Ultra field emission SEM instrument equipped with an EDXS attachment (Oxford).

### 2.1.3 Thermal gravimetric analysis

Thermal gravimetric analysis (TGA) is a technique which can provide thermal decomposition temperatures, component information and phase transformation of synthesized composite. The analysis is usually conducted on an instrument referred to a thermogravimetric analyzer that can continuously measure mass while the temperature is changed over time. Usually, the temperature is increased in a linear way, a standard temperature program of 10 °C/min ramp was used in this thesis. The weight percentage of sulfur can be determined by the TGA device at a range of 200-400$^{o}$C, which is presented in a typical thermal gravimetric analysis (TGA) analysis curve of GO-wrapped sulfur composite in **Figure 2.2**.[49] Thermal gravimetric analysis (TGA) in this thesis was performed under constant nitrogen flow on a TA Instruments (SDT Q500 analyzer).

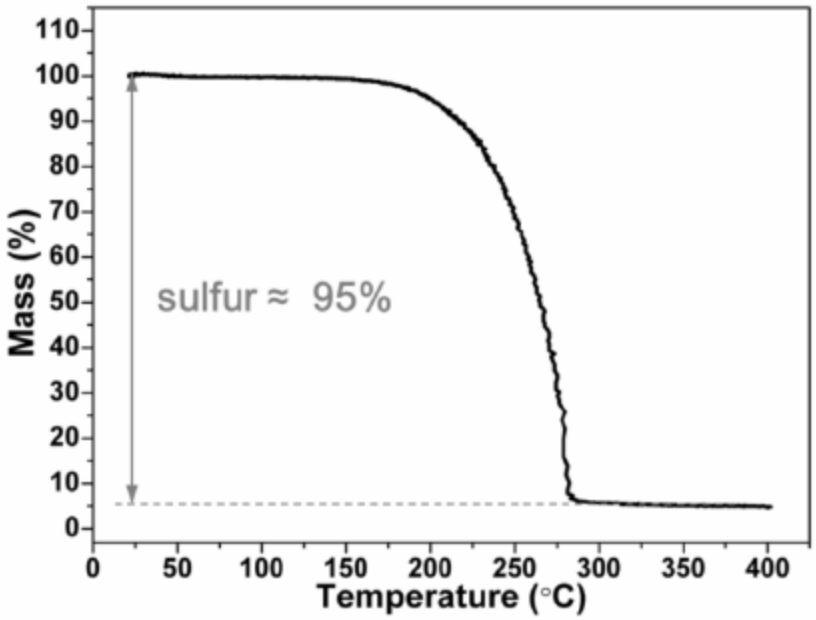


**Figure 2.2** A typical thermal gravimetric analysis (TGA) analysis curve of GO-wrapped sulfur composite, reproduced with permission from reference 49.

### 2.1.4 Electronic conductivity measurement

The four-point probe technique is used to measure approximate electronic conductivity of synthesized materials. The four-point probe instrument has two pairs of electrodes. Two outer probes are called current-carrying electrodes while two inner probes are called voltage-sensing electrodes, as shown in **Figure 2.3**.[50] A current passes through two current-carrying probes and induces a voltage in the inner voltage probes, which allows the measurement of the substrate resistivity. The four-point probe can make more accurate measurements compared with conventional two-point probe since it can exclude the voltage drop from the measuring wires. In order to measure the bulk conductivity of powder samples with four-point probe, powders are usually pressed into pellets. Electronic conductivity of the powder samples in this thesis was measured on a Jandel four-point

probes connected with RM3000 test unit.

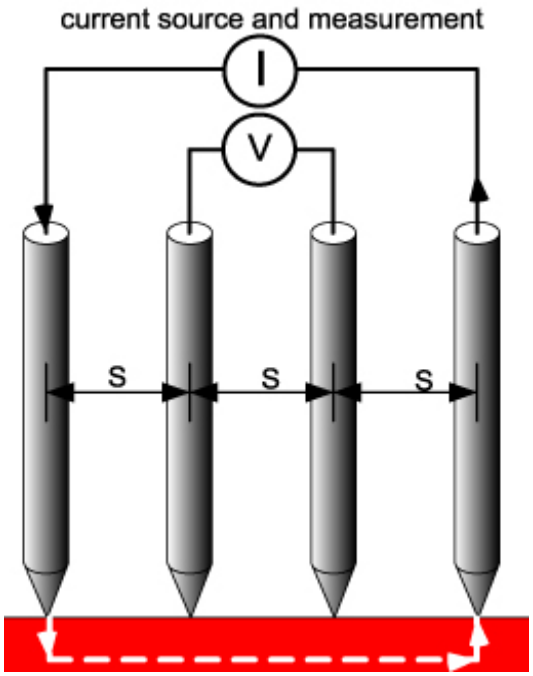


**Figure 2.3** Illustration of a typical four-point probe, reproduced with permission from reference 50.

## 2.2 Electrochemical techniques and measurements

### 2.2.1 Solid-state cell configuration

A cross-section view of solid-state cell with three components is shown in **Figure 2.4**.[51] The positive electrode consists of active material, ionic conductor, and electronic conductor while the lithium-indium alloy or lithium metal serves as the negative electrode. A layer of Li-ion conducting solid electrolyte materials separates two electrodes. In order to ensure three components (cathode, solid electrolyte layer, anode) have intimate contact with each other, an external pressure is usually applied on the cell.

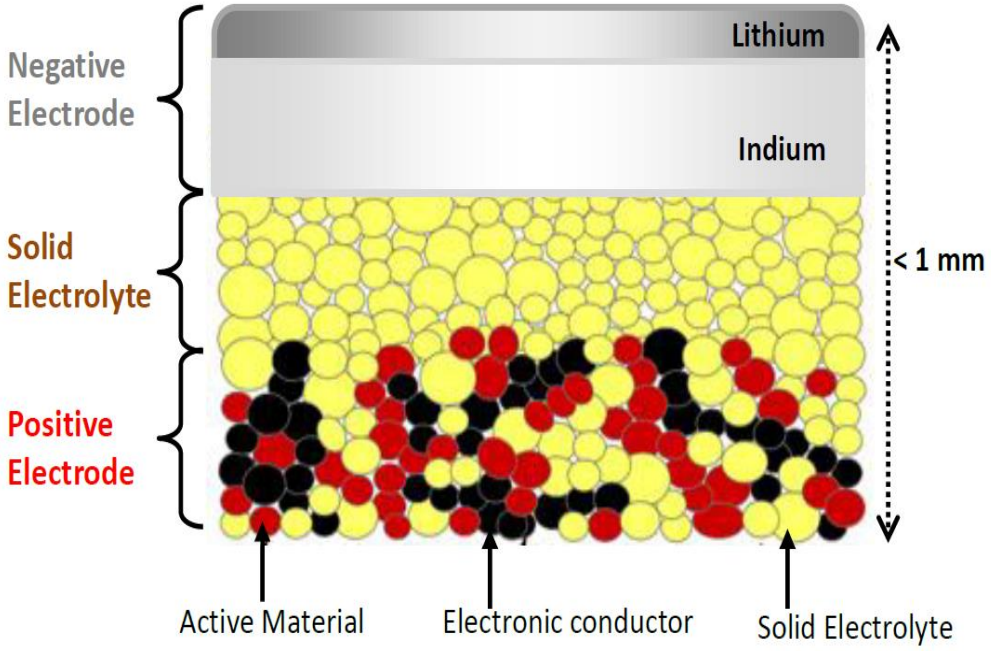


**Figure 2.4**: Schematic illustration of cross-section of a solid-sate battery, reproduced with permission from reference 51.

To carry out the electrochemical performance of solid-state cell, a home-designed cell (**Figure. 2.5**) was assembled in an argon-filled glovebox. First, ~80 mg of solid electrolyte was placed in a polycarbonate cylinder and pressed between two stainless steel current collectors at 120 MPa. Next, 2-5 mg of the cathode composite materials were added, and the cell was cold-pressed for 3 min under a pressure of 360 MPa. Then, the Li/In foil (or Li metal) was placed on the opposite side and the three-layered pellet was pressed at 100 MPa. Finally, the cell was tightened by screws with applying a torque of 9.6 N·m.

### 2.2.2 Galvanostatic cycling

Galvanostatic cycling is a commonly used electrochemical technique to characterize capacity and cycle life of cell. In galvanostatic cycling, a constant current is applied to the cell until it discharges to the lower cut-off voltage. Then, the current is reversed and the

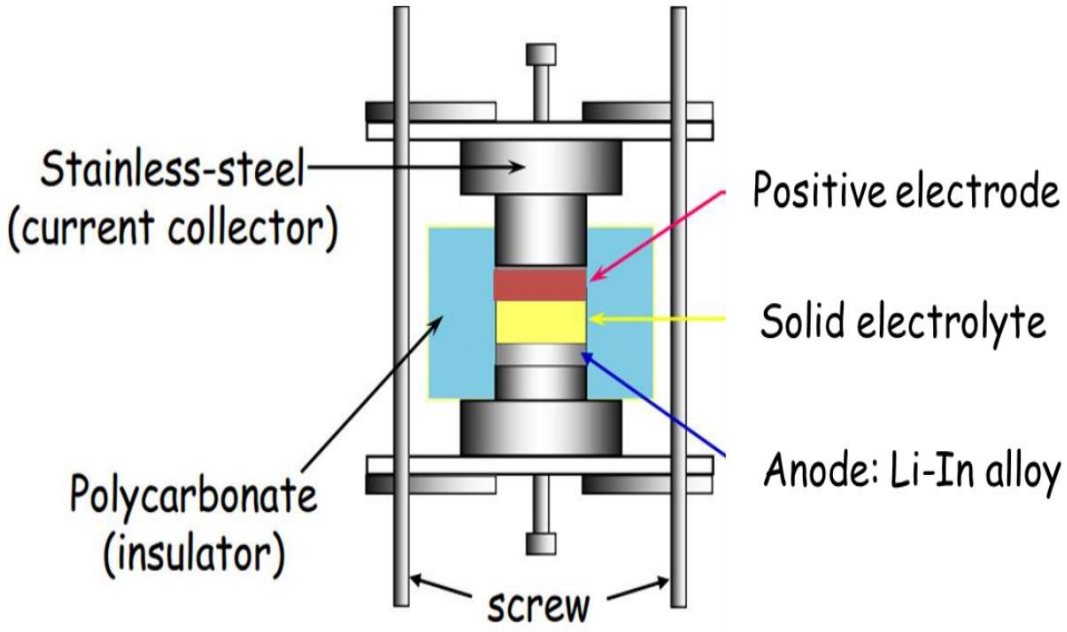


**Figure 2.5** Illustration of an all-solid-state battery cell, reproduced with permission from reference 51.

cell charges until reaching the upper cut-off voltage. Within cycling, the voltage of the cell is recorded as a function of capacity delivered. Based on these data, the curve of voltage *versus* capacity can be plotted, which presents the information of battery performance. The overall capacity corresponds to the final point reaching the cut-off voltage. A single-phase reaction usually relates to that voltage is linearly dependent on capacity while a two-phase reaction corresponds to a plateau of potential irrespective to capacity. Long-term cycling performance is evaluated by the specific capacity retained after certain cycle numbers. Rate capability of a cell is evaluated by comparing the battery cycling performances at a variety of current densities. Good rate capability means cells do not have huge capacity change when applying high current density. The galvanostatic cycling was carried out using a VMP-3 potentiostat/galvanostat station (Bio-Logic Science Instruments).

### 2.2.3 Cyclic voltammetry

Cyclic Voltammetry (CV) is an electrochemical technique which is performed by swapping the potential of a working electrode and measuring the resulting current. In a cyclic voltammetry experiment, the working electrode potential is ramped linearly with time. Once the voltage reaches its upper or lower limit, it is reversed. When the voltage increases, oxidation reaction occurs around certain voltage. The reduction reaction happens reversely. Generally, this technique can quickly provide clear information about the redox reactions. CV measurements in this thesis were carried out on a VMP-3 potentiostat/galvanostat station (Bio-Logic Science Instruments).

### 2.2.4 Electrochemical impedance spectroscopy

Electrochemical impedance spectroscopy (EIS) is an electrochemical technique that measures the impedance of materials, which by definition is the ability to resist the flow of electrical current. In an EIS analysis, an alternating current (AC) voltage within a wide range of frequencies is applied to a cell and the current response is measured. The small amplitude of the voltage applied on cell enables a linear response from the cell which composed of multiple non-linear electric elements. The response current signal is measured and can be analyzed as a sum of sinusoidal functions. In this case, the impedance can be described by a complex value consisting of a real part and an imaginary part at each measured frequency.

Nyquist plot is plotted with the imaginary part of the resistance on y-axis and the real part on x-axis. **Figure 2.6** below illustrates a typical Nyquist plot for a solid ionic conductor. When the semi-circle is not clear to identify in the measurements, the value of

the resistance can be obtained by extrapolation of the linear part to the x-axis. In this thesis, EIS measurements were carried out on a VMP3 station with EIS/Z capabilities (Bio-Logic Science Instruments). The DC voltage was kept at open-circuit voltage and the AC voltage of 5 mV in amplitude was applied with a frequency of 1 MHz-0.1Hz.

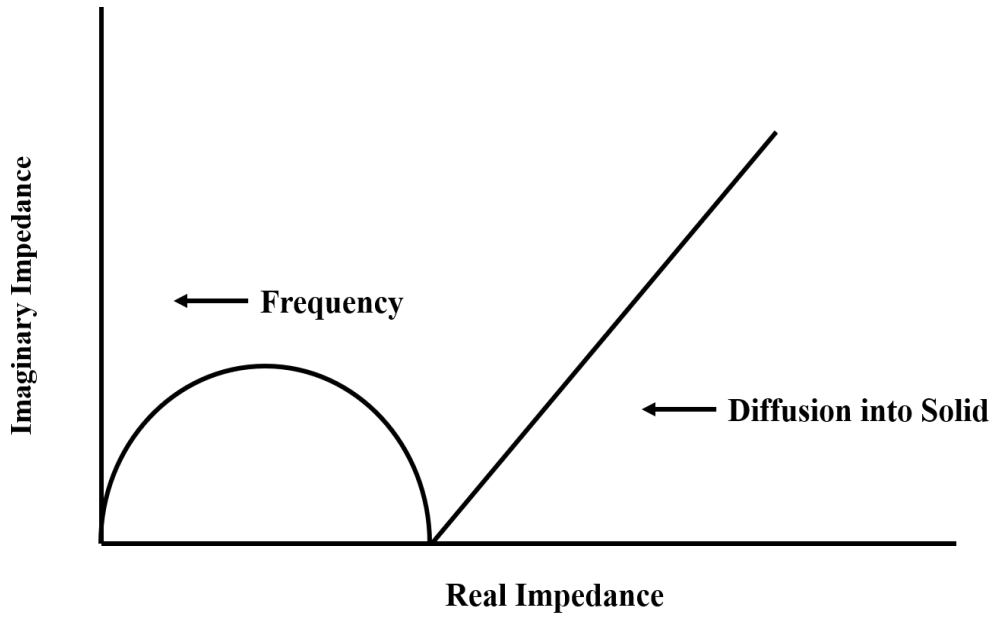


**Figure 2.6** A typical Nyquist plot of impedance measurement on solid electrolyte.

# Chapter 3: A high capacity all solid-state Li-S battery enabled by conversion-intercalation hybrid cathode architecture

## 3.1 Introduction

As mentioned in **chapter 1**, it is well acknowledged that the commercialization of Li-S technology in liquid electrolyte cells is still challenging. The main problems concerning cathode design in conventional Li-S battery lie in suppressing polysulfide dissolution and diffusion into electrolyte, which can be systematically solved by solid state system. Substitution of the organic electrolyte for solid-state electrolytes (SSEs) that show zero solubility for polysulfides, and which can support the solid-solid sulfur/lithium sulfide conversion reaction is an alternative approach to resolve some of the above challenges.[52-55] The mechanism for $Li^+$-ion transport within the cathode that supports sulfur redox in solid-state batteries differs from that in conventional batteries using liquid electrolytes. Because both electrode and electrolyte are solid, and close high surface-area contact of the two materials is necessary, a significant fraction of SSE in the cathode layer is usually needed to provide an efficient $Li^+$-ion conductive pathway.[55] In this regard, thiophosphates are one of the most widely used SSE materials in all-solid-state Li-S cells owing to their excellent ductility coupled with good ionic conductivity.[56-57] However, because high surface area carbonaceous materials are also required in sulfur cathodes – to provide the requisite electrical contact for electron transfer to sulfur – their contact with the thiophosphate electrolyte can lead to decomposition of the SSE *via* oxidation on charge.[58-

[61] This results in poor Coulombic efficiency, especially in the initial cycles until an insulating passivation layer is formed.[58,61]

Sulfur hosts that function as alternatives to carbon, and encompass both good electronic and ionic conductivity can address these difficulties, such as transition metal sulfides ($M_xS_y$, M = V, Ti, Fe, Ni, Mo, *etc.*).[62-65] Some of these materials not only display excellent electronic conductivity (comparable to, or better than carbonaceous materials), but also good Li-ion diffusion properties and chemical stability, and interfacial compatibility with sulfur/thiophosphate materials.[66-67] They can also be involved in electrochemical reactions with lithium based on a dual insertion/conversion mechanism and hence contribute additional capacity.[64,68] These principles are beautifully exemplified in a recent report by Passerini *et al.* of a C/$FeS_2$/S/SSE composite cathode using 30 wt. % active material (S + $FeS_2$), that was reported to deliver an areal capacity up to 3.5 $mA \cdot h \cdot cm^{-2}$ in an all-solid-state Li-S cell.[69] Oxidation of the solid electrolyte (amorphous $Li_3PS_4$:LiI) on initial charge of the cell led to overcharge and low coulombic efficiency, but the latter improved upon cycling once a passivation layer formed.

Unlike iron sulfide which adopts a pyrite structure, vanadium disulfide exhibits a layered structure where the vanadium is octahedrally coordinated with sulfur atoms to form two-dimensional sheets.[70] The $VS_2$ sheets are bound together by weak van der Waals interlayer interactions. Within the sheets, electrons are highly delocalized in the overlapping, dangling V 3d and S $2p_z$ orbitals, leading to the material's metallic properties, and an electron conductivity in the range of 1000 $S \cdot cm^{-1}$.[70] $VS_2$ also features a low $Li^+$ migration barrier (0.22 eV) compared to many other redox-active transition metal disulfides.[71-72] For these reasons, it has been utilized as a cathode material in Li-ion

batteries, where it is shown to exhibit a theoretical capacity of 233 $mA \cdot h \cdot g^{-1}$ within the electrochemical window from 1.4 – 3.1 V *vs.* $Li/Li^+$, and good structural stability during (de)lithiation.[73] While the open layered $VS_2$ structure provides excellent electronic conductivity and facilitates $Li^+$ ion transport in Li-ion cells, these factors also aid the solid-solid $S/Li_2S$ redox process as described below.

Here I report a rational design of a sulfur/nano-$VS_2$ hybrid cathode for high capacity solid-state Li-S batteries. In combination with a thiophosphate solid electrolyte (β-$Li_3PS_4$), the sulfur cathode composite ($S/VS_2$/β-$Li_3PS_4$) features multi-channel electronic and ionic conductive networks and achieves excellent sulfur utilization at a high active material (S + $VS_2$) loading of 60 wt. %, double that of the $FeS_2$/S battery. Our solid-state Li-S/$VS_2$ cells delivered a reversible specific capacity of 1444 $mA \cdot h \cdot g^{-1}$ based on S (or 640 $mA \cdot h \cdot g^{-1}$ based on S and $VS_2$) at an active loading of 1.7 $mg_{S+VS2} \cdot cm^{-2}$. This translates to a sulfur utilization of ~85 %. A stable areal capacity up to 7.8 $mA \cdot h \cdot cm^{-2}$ was also achieved at a very high active material loading of 15.5 $mg \cdot cm^{-2}$. To the best of our knowledge, this is the first report of a solid-state Li-S battery which utilizes a metallic transition metal sulfide as a host material that exhibits excellent sulfur utilization, stable cycling, and overall coulombic efficiencies close to 100%. The whole chapter 3 is reproduced with permission from S. Xu, C. Y. Kwok, L. Zhou, Z. Zhang, I. Kochetkov, and L. F. Nazar. A High Capacity All Solid-State Li-Sulfur Battery Enabled by Conversion-Intercalation Hybrid Cathode Architecture. *Adv. Funct Mater.* **2021,** *31,* 2004239.[74]

## 3.2 Experimental methods

*Synthesis of $VS_2$.* $VS_2$ was prepared by a one-pot hydrothermal method.[63,73] Namely, 2

mmol ammonium metavanadate ($NH_4VO_3$, 98.5%, AnalaR NORMAPUR) was dissolved in an aqueous ammonia solution (28 wt. %, Sigma-Aldrich), and thioacetamide (ACS grade, Sigma-Aldrich) was then added. The molar ratio between the vanadium and sulfur precursors was approximately 1:5. The homogenous solution was then transferred to a Teflon-lined autoclave and maintained at 165 ºC for 20 hours under static conditions. The black $VS_2$ solid was rinsed with water and ethanol, then collected after drying at 90 ºC in a vacuum oven for 12 hours.

*Preparation of the hybrid cathode composite.* Elemental sulfur was melt-diffused into $VS_2$ at 160 °C for 12 h to afford the $S/VS_2$ composite with a sulfur content of 33 wt. %, as determined by thermogravimetric analysis (TGA). The solid-state electrolyte (SSE), β-$Li_3PS_4$ was prepared by vacuum drying the raw material ($Li_3PS_4 \cdot 3THF$, BASF) in a Büchi vacuum oven at 150 °C for 48 h before transfering it to an Ar-filled glovebox. The final cathode composite material was prepared by a physical blend of the $S/VS_2$ composite material and SSE with a ratio of 6:4 in an Ar-filled glovebox. For comparson, $S/C/Li_3PS_4$ composite cathode was also prepared using the same method using carbon black (Vulcan XC 72R) as sulfur host material.

*Physical characterization.* SEM studies were carried out on a Zeiss Ultra field emission SEM instrument equipped with an EDXS attachment (Oxford). XRD data were collected on a PANalytical Empyrean instrument outfitted with a PIXcel two-dimensional detector operating at 45 kV/40mA, using Cu-Kα radiation (λ = 1.5405Å). TGA, used to determine the sulfur content of the materials, was carried out on a TA Instruments SDT Q500 at a heating rate of 5 $°C \cdot min^{-1}$ under $N_2$ flow.

*Electrochemical studies.* The electrochemical performance of the solid-state Li-S

battery was carried out using a home-designed cell, which was assembled in an Ar-filled glovebox. A cylindrical die with an internal diameter of 10 mm was used for pellet preparation. In a typical procedure, approximately 70 mg of the solid electrolyte powder was first pressed between two stainless steel rods. The cathode composite material ($S/VS_2/Li_3PS_4$ or $S/C/Li_3PS_4$) was then added to the cathode compartment and further pressed alongside the SSE pellet for several minutes. Next, Li foil or Li/In alloy was placed in the anode compartment. Finally, the die was placed in an air-tight stainless-steel casing capable of maintaining constant pressure on the pellet. Screws on the casing were fastened by applying a torque of 9.6 N·m. All electrochemical studies were carried out on a Bio-logic VMP3 electrochemical station. Cyclic voltammetry and EIS studies were carried out at a scan rate of 0.02 $mV \cdot s^{-1}$ and an amplitude of 5 mV in the frequency range of 200 mHz to 200 kHz, respectively. Galvanostatic cycling was performed in the potential range of 1.4 – 3.1 V *vs.* $Li/Li^+$, where the molar ratio of Li:In (maintained at < 1) fixes the voltage of the negative Li-In alloy electrode at -0.6 V *vs.* $Li/Li^+$.[75] The theoretical capacity of the $S/VS_2$ hybrid cathode is 713 $mA \cdot h \cdot g_{VS2+S}^{-1}$ at a $S:VS_2$ weight ratio of 1:2.

## 3.3 Results and discussion

$VS_2$ was prepared *via* a hydrothermal reaction using thioacetamide and ammonium vanadate as precursors.[63,73] Scanning electron microscopy (SEM) analysis **(Figure 3.1 a)** reveals the platey $VS_2$ crystallites self-assemble to form flower-like aggregates with diameters of 10 - 20 μm (**Figure 3.1 a-inset**). The lamellar structures in the aggregates are comprised of ~100 nm thick $VS_2$ nanoplates consisting of stacked $VS_2$ atomic layers (**Figure 3.1 b**). The X-ray diffraction (XRD) pattern in **Figure 3.1 c** reveals $VS_2$ (ICSD-

98-008-6519) is present as the only crystalline component.[76]

The successful infiltration of elemental sulfur into the $VS_2$ nanoplate aggregates *via* melt-diffusion was evidenced by the change in the composite ($S/VS_2$) morphology (**Figure 3.1 d**), with respect to the pristine $VS_2$ nanoplates (**Figure 3.1 b**). The rough surface observed on the $S/VS_2$ lamella and the diminished gaps between the clumped nanoplates (**Figure 3.1 e**) suggests the $VS_2$ layers are (at least partially) covered by sulfur. Thermogravimetric analysis (**Figure 3.1 f**) determined that the elemental sulfur content of the $S/VS_2$ composite was 33 wt. %. Sulfur coating of the underlying metallic $VS_2$-sheet

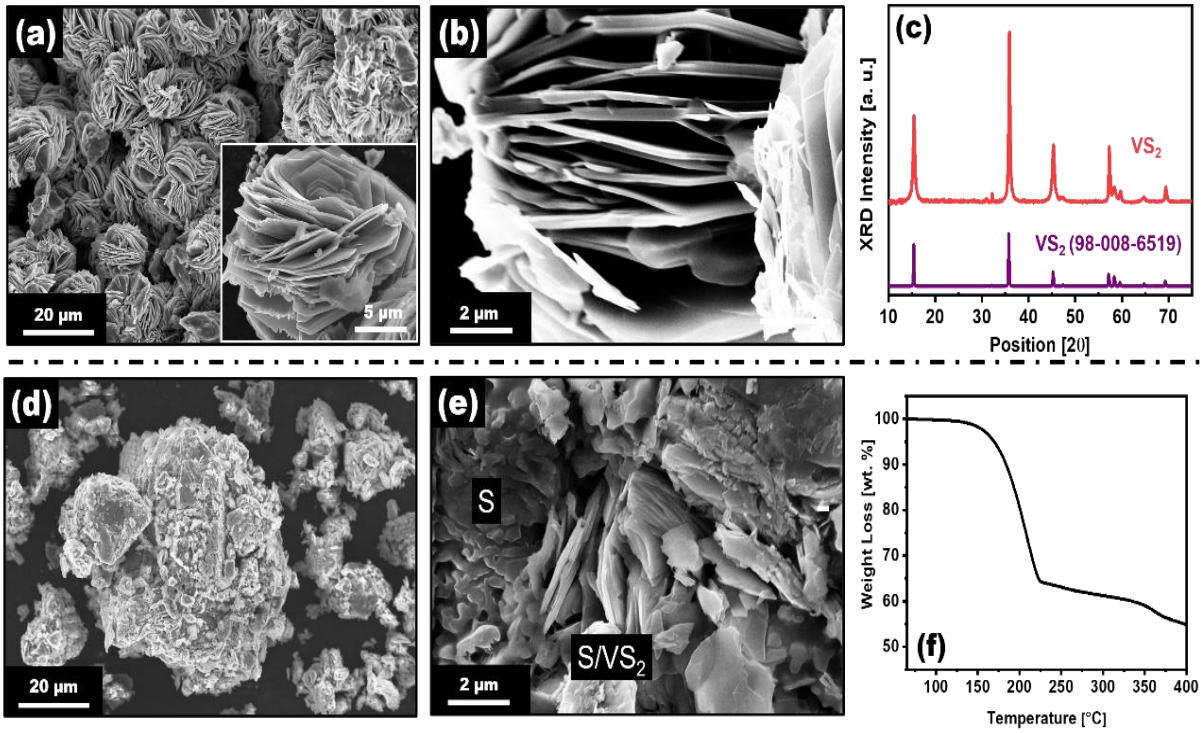


**Figure 3.1** Characterization of (a-c) $VS_2$ and (d-f) the $S/VS_2$ composite. (a-b) SEM images and (c) XRD pattern for $VS_2$; (d-e) SEM images and (f) TGA curve for the $S/VS_2$ composite, yielding a sulfur content of ~33 wt. % at a ramp rate of 5 ˚C·min$^{-1}$ under $N_2$ flow.

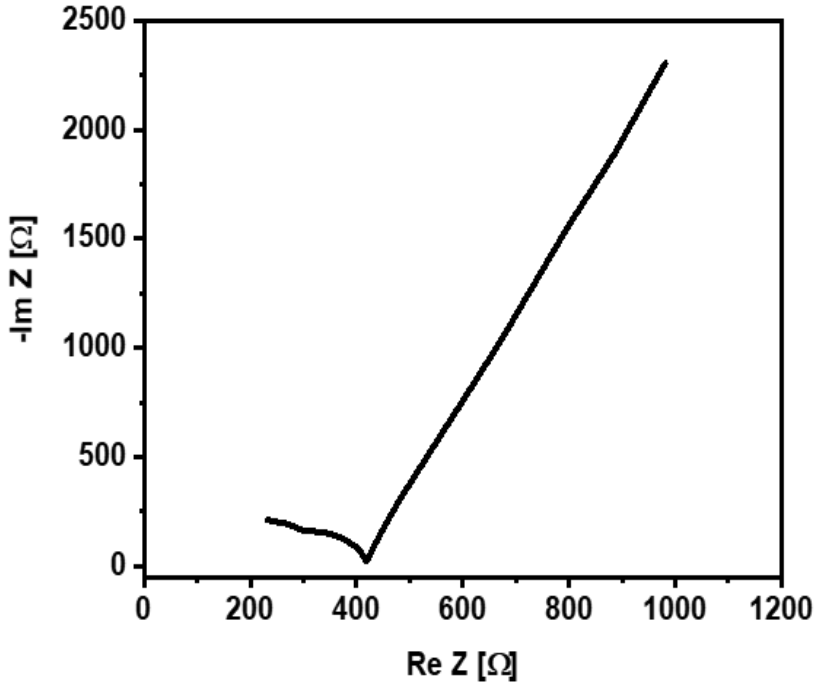


**Figure 3.2** Nyquist plot of the β-$Li_3PS_4$ electrolyte measured at 25 ºC. The ionic conductivity was determined to be 0.23 $mS \cdot cm^{-1}$ from the Warburg impedance contribution at low frequency.

skeleton accounts for a quasi-core shell morphology that provides the necessary electronic pathway for electron transfer to sulfur when the materials are pressed together to form a composite cathode. In addition, the small gaps between the individual $S/VS_2$ plates create a buffer void for sulfur expansion to maintain structural integrity of the electrode when $Li_2S$ is formed during discharge. This composite material, when intimately mixed with the solid electrolyte, enables electronic and ionic avenues that lead to high sulfur utilization during the $S \leftrightarrow Li_2S$ conversion reaction as described below.

$Li_3PS_4$ was selected as the solid electrolyte due to its reasonably good ionic conductivity (0.23 $mS \cdot cm^{-1}$, **Figure 3.2**).[77] The moderate ductility of $Li_3PS_4$ enables fabrication of the sulfur cathode composite ($S:VS_2:Li_3PS_4$ at a 2:4:4 weight ratio) by

mixing the $Li_3PS_4$ powders with the $S/VS_2$ hybrid active materials *via* physical blending.[78] This approach preserves the $S/VS_2$ core-shell architecture (**Figure 3.1 e**) while achieving intimate contact between the SSE and the $S/VS_2$ materials. SEM and energy dispersive X-ray spectroscopy (EDX) analysis demonstrate that all three components are evenly distributed (**Figure 3.3**). Thus, with judicious cathode design – by coating the insulating sulfur layer onto the $VS_2$ nanoplates prior to mixing them with the solid electrolyte – direct contact between β-$Li_3PS_4$ and metallic $VS_2$ is minimized. This is beneficial to limit solid electrolyte oxidation as we show below.

We examined the electrochemistry of the sulfur cathode in a solid-state battery

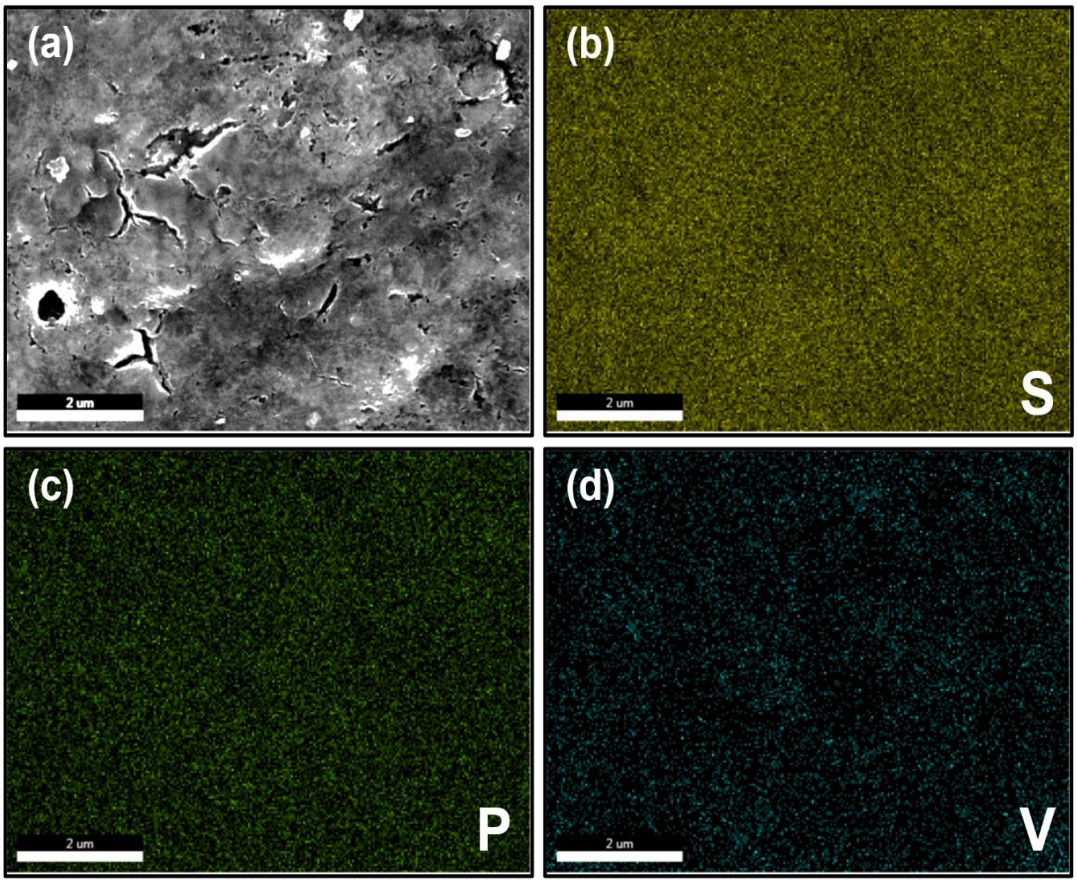


**Figure 3.3.** EDX analysis of the $S/VS_2/Li_3PS_4$ cathode composite material. (a) SEM; (b-d) elemental mapping of (b) S; (c) P; and (d) V.

utilizing Li/In alloy (or lithium metal) as anode, and β-$Li_3PS_4$ as the solid-state electrolyte separator. The well-defined and relatively symmetric cyclic voltammetry (CV) profile indicates good electrochemical reversibility of the S/$VS_2$ cathode (**Figure 3.4 a**). In the CV profile, a pair of redox peaks is clearly identified though an additional shoulder was also observed in. While two redox couples are expected, since both sulfur-conversion ($2Li + S \leftrightarrow Li_2S$) and Li-intercalation reactions in $VS_2$ ($Li + VS_2 \leftrightarrow LiVS_2$) potentially take place, the obvious peaks (~1.1 V and 2.0 V *vs.* Li/In) correspond to the redox reaction of S while the vague shoulders (~1.6 V and 1.8 V *vs.* Li/In) may correspond to the redox reaction of $VS_2$. In **Figure 3.4 b**, the hybrid cathode exhibits similar galvanostatic charge/discharge profiles to those in other solid-state Li-S cells.[52,54] We attribute this to the likely similar thermodynamic potentials of the two active materials.[54,73] To gain insight into the redox mechanism, we conducted *ex-situ* XRD analysis on the hybrid cathode at different stages of (dis)charge (**Figure 3.4 b-c**). The peak of $VS_2$ at 15˚ was very vague after mixing with solid electrolyte, thus a range of 2θ from 25˚ to 60˚ was shown here. Initially (**Figure 3.4 c-A**), the pristine cathode composite exhibits three reflections associated with the interlayer reflections of $VS_2$ while those for the crystalline sulfur are indistinguishable from $Li_3PS_4$ due to their similar XRD patterns within this region. When the cell was discharged to 0.8 V *vs.* Li/In (equivalent to 1.4 V *vs.* $Li/Li^+$) (**Figure 3.4 b-C**), the $VS_2$ XRD reflections (located at 36˚ (011), 46˚ (102), and 58˚ (103) in **Figure 3.4 c-A**) shift toward much lower angles (**Figure 3.4 c-C**). This accounts for approximately a 6 % increase in the *a* and *c* lattice parameters of $VS_2$ (SG: *P*-3m1) due to $Li^+$ insertion and formation of isostructural $LiVS_2$ (ICSD-98-064-2325). Meanwhile, two new peaks at 27º and 45º in **Figure 3.4 c-C** were identified as $Li_2S$, resulting from sulfur conversion to lithium sulfide. When the cell

was charged to 2.5 V *vs.* Li/In, the phase evolution (C → E in **Figure 3.4 c**) of both materials show that their respective pristine counterparts are recovered (**Figure 3.4 c-E**).

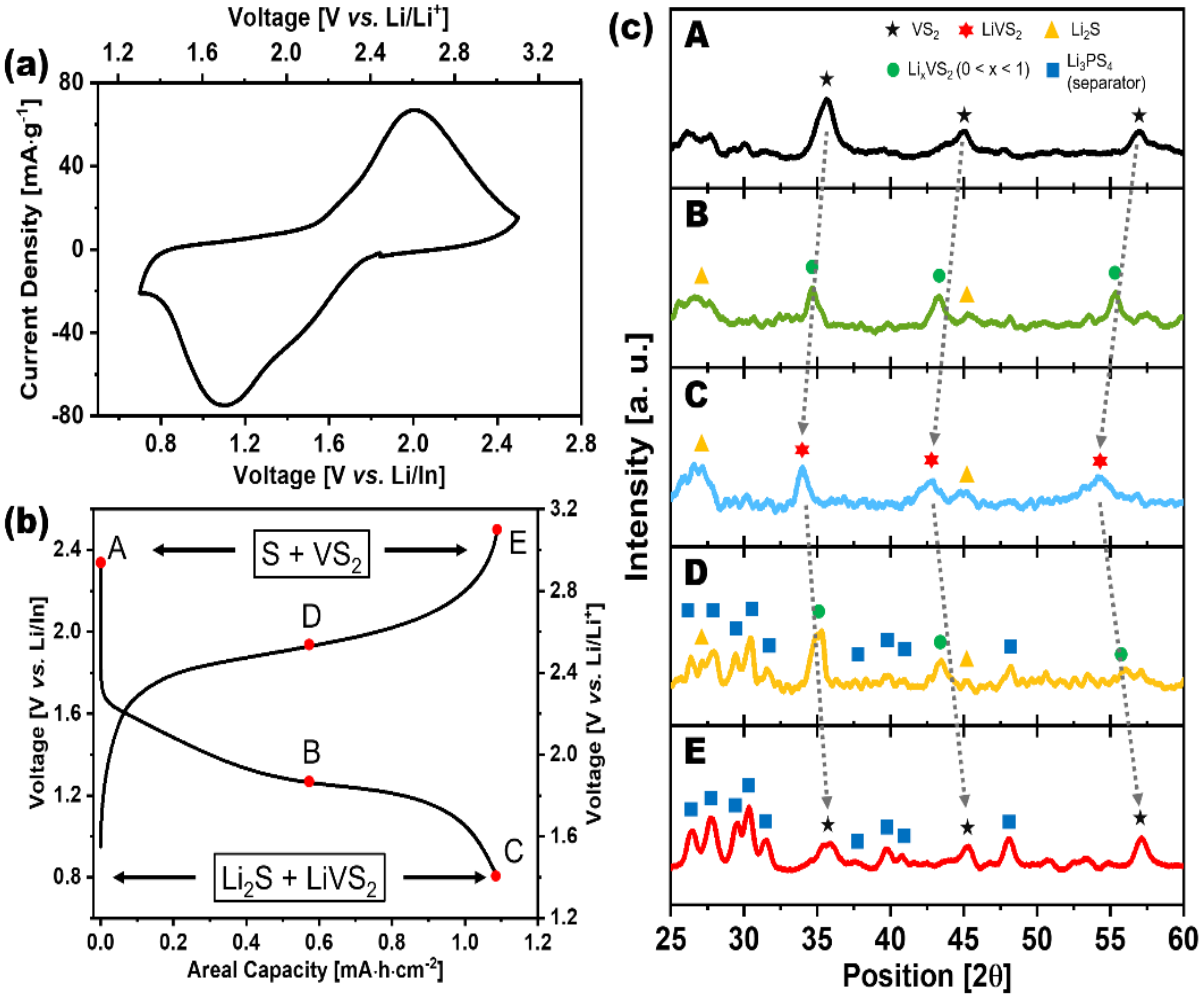


**Figure 3.4** Investigation in the electrochemical mechanism for the solid-state Li-S/$VS_2$ battery. (a) CV profile of the S/$VS_2$/$Li_3PS_4$|SE|Li/In cell. (b) Electrochemical profile and (c) *ex-situ* XRD for the same battery at different stages of (dis)charge collected at a current rate of 0.12 mA·$cm^{-2}$ (C/10). The $Li_3PS_4$ reflections in panels D & E are due to the underlying solid electrolyte layer that could not be fully detached from the cathode material. The grey arrow shows the peak evolutions of $VS_2$ to $LiVS_2$ during discharge and vice-versa during charge.

Interestingly, the intermediate stages of the discharge and charge processes (panel B and D in **Figure 3.4 c**, respectively) reveal the co-existence of $Li_xVS_2$ and $Li_2S$. We conclude that the electrochemical mechanism of the Li-S/$VS_2$ battery follows a conversion/(de)lithiation process, in agreement with CV profile in **Figure 3.4 a**. Moreover, quantitative analysis of the electrochemical data clearly shows the $VS_2$ cannot account for the capacity offered by the cell in **Figure 3.4 b** (see **Electrochemical Analysis** below). Thus, both sulfur and vanadium disulfide are involved in the redox process. In summary, the solid electrolyte $Li_3PS_4$ serves as the main ionic conductor to deliver $Li^+$ ions for S/$Li_2S$ redox, and metallic $VS_2$ functions as the electronic conductor to deliver electrons. However, because lithiated vanadium sulfide ($Li_xVS_2$) is also a mixed ion/electron

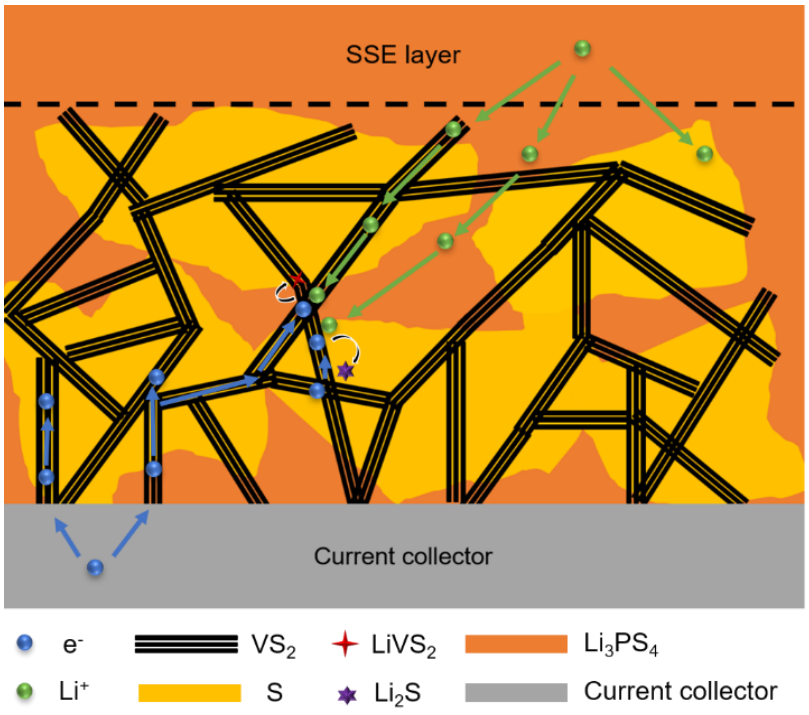


**Figure 3.5** Schematic diagram illustrating the proposed microstructure and discharge mechanism for the solid-state hybrid Li-S/$VS_2$ battery.

conductor and exhibits good Li-ion mobility between the $VS_2$ atomic layers, [79] it can serve as an additional role as a Li-ion delivery vehicle when it is formed midway through discharge and charge (*i.e.*, $Li_xVS_2 + S \leftrightarrow Li_2S + VS_2$). This concept is illustrated schematically in **Figure 3.5**; the precise nature of the mechanism will be the subject of future studies.

*Electrochemical Analysis*

The solid-state Li-S/$VS_2$ cell illustrated in **Figure 3.7 b** exhibited a capacity of 0.86 mA·h. The active material loading of 1.35 $mg_{(S+VS2)}$ contained 67 wt. % $VS_2$. If sulfur is assumed not to take part in the redox process, the $VS_2$ gravimetric capacity would be 0.86 mA·h ÷ 0.9 mg = 956 $mA{\cdot}h{\cdot}g^{-1}$, far exceeding its theoretical value of 233 $mA{\cdot}h{\cdot}g^{-1}$. Even if $Li_3PS_4$ is assumed to participate in the redox instead of sulfur, it would only account for ~170 $mA{\cdot}h{\cdot}g^{-1}$, contributing a total capacity of 170 $mA{\cdot}h{\cdot}g^{-1}$ × 0.9 mg = 0.153 mA·h. In that case, $VS_2$ gravimetric capacity would be (0.86 - 0.153) mA·h ÷ 0.9 mg = 785 $mA{\cdot}h{\cdot}g^{-1}$, still exceeding its theoretical value. This concludes that sulfur and $VS_2$ must be involved in the redox process.

*Calculation for Sulfur Utilization*

The highest capacity achieved for the S/$VS_2$/$Li_3PS_4$|SE|Li-In cell was measured to be 0.86 mA·h at an active material loading of 1.35 $mg_{(S+VS2)}$ (**Figure 3.7 b**). TGA (**Figure 3.1 d**) reveals the sulfur content in the S/$VS_2$ hybrid cathode composite was ~33 wt. %. Considering the theoretical capacity of $VS_2$ within the electrochemical window for sulfur redox is 233 $mA{\cdot}h{\cdot}g^{-1}$, based on a one $Li^+/e^-$ insertion mechanism ($Li^+ + e^- + VS_2$ →

$LiVS_2$), the capacity contributed by $VS_2$ alone is 233 $mA \cdot h \cdot g^{-1}$ × 0.9 mg = 0.21 mA·h. In that case, the capacity contributed by S is at least 0.65 mA·h. Thus, the specific capacity contributed by sulfur is 0.65 mA·h ÷ 0.45 mg = 1444 $mA \cdot h \cdot g^{-1}$. This translates to a sulfur utilization of approximately 85 %.

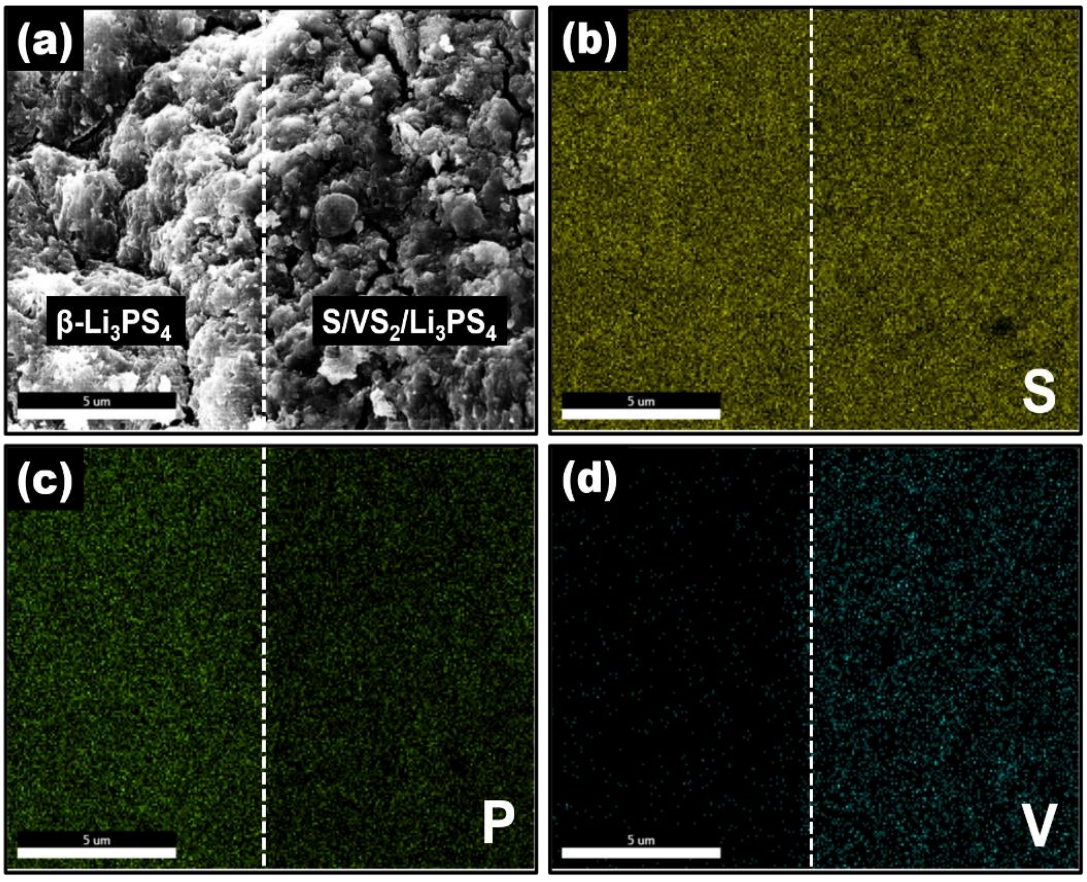


**Figure 3.6** Analysis of the interface between $Li_3PS_4$ (left) and $S/VS_2/Li_3PS_4$ (right) after 10 cycles at C/10. (a) SEM image of the area; (b-d) EDX elemental mapping of (b) S; (c) P; and (d) V.

Good interfacial stability of the components in the cathode layer and the thiophosphate in the solid electrolyte layer is another important parameter for the longevity of solid-state batteries. The components in the Li-$S/VS_2$ cathode and SSE layers do not mix

after cycling, as evidenced by the clear boundary between the two layers determined by cross-section EDX analysis after cycling for 10 cycles at C/10 (**Figure 3.6 a-d**). Sulfur and phosphorus are observed in both the cathode and electrolyte layers owing to the presence of sulfur and $Li_3PS_4$ (**Figure 3.6 b-c**), whereas no vanadium is detected in the electrolyte layer (**Figure 3.6 d**), indicating that no elemental diffusion occurs, as expected. In contrast, literature reports show that thiophosphates form an unstable interface with all lithium transition metal oxides on cycling: for example, in a $LiCoO_2|Li_2S/P_2S_5$ solid-state Li-ion cell, mutual diffusion of Co, P, and S at the cathode-SSE interface and electrochemical oxidation of the thiophosphate on charge [80] result in formation of a high impedance interlayer and subsequent cell degradation.[81-83]

The long-term electrochemical performance of solid-state Li-S/$VS_2$ cells was examined by galvanostatic cycling at 25 °C. **Figure 3.7 a** displays the performance of the S/$VS_2$ cathode at an areal loading of 1.7 $mg_{S+VS2} \cdot cm^{-2}$ at a current density of 0.12 $mA \cdot cm^{-2}$ (equivalent to a rate of C/10). The cathode exhibited an initial discharge capacity of 0.88 $mA \cdot h \cdot cm^{-2}$. A high initial CE of 96 % was achieved after recharging the cell to 2.5 V. The very high CE achieved in the first cycle – in contrast to other solid-state Li-S batteries where values as low as 80% have been observed [57,69,84] – is attributed to the minimal contact between the metallic $VS_2$ and the solid electrolyte in the cathode layer, as well as to the electronic conductivity and additional Li-ion delivery pathways provided by $VS_2$ (**Figure 3.5**). The hybrid cathode reached a specific capacity of 640 $mA \cdot h \cdot g_{(S+VS2)}^{-1}$ after several activation cycles, while the CE reached nearly 100 % and remained stable hereafter. After subtracting the capacity contribution from $VS_2$ (see **Sulfur Utilization** for calculations), the specific capacity of sulfur was estimated to be 1444 $mA \cdot h \cdot g^{-1}$, which

corresponds to a high sulfur utilization of ~85 %. An areal capacity of ~1 mA·h·cm$^{-2}$ was achieved using this configuration, and stable reversible redox behavior was observed (**Figure 3.7 b**). We also examined the plausibility of utilizing Li metal as the anode to

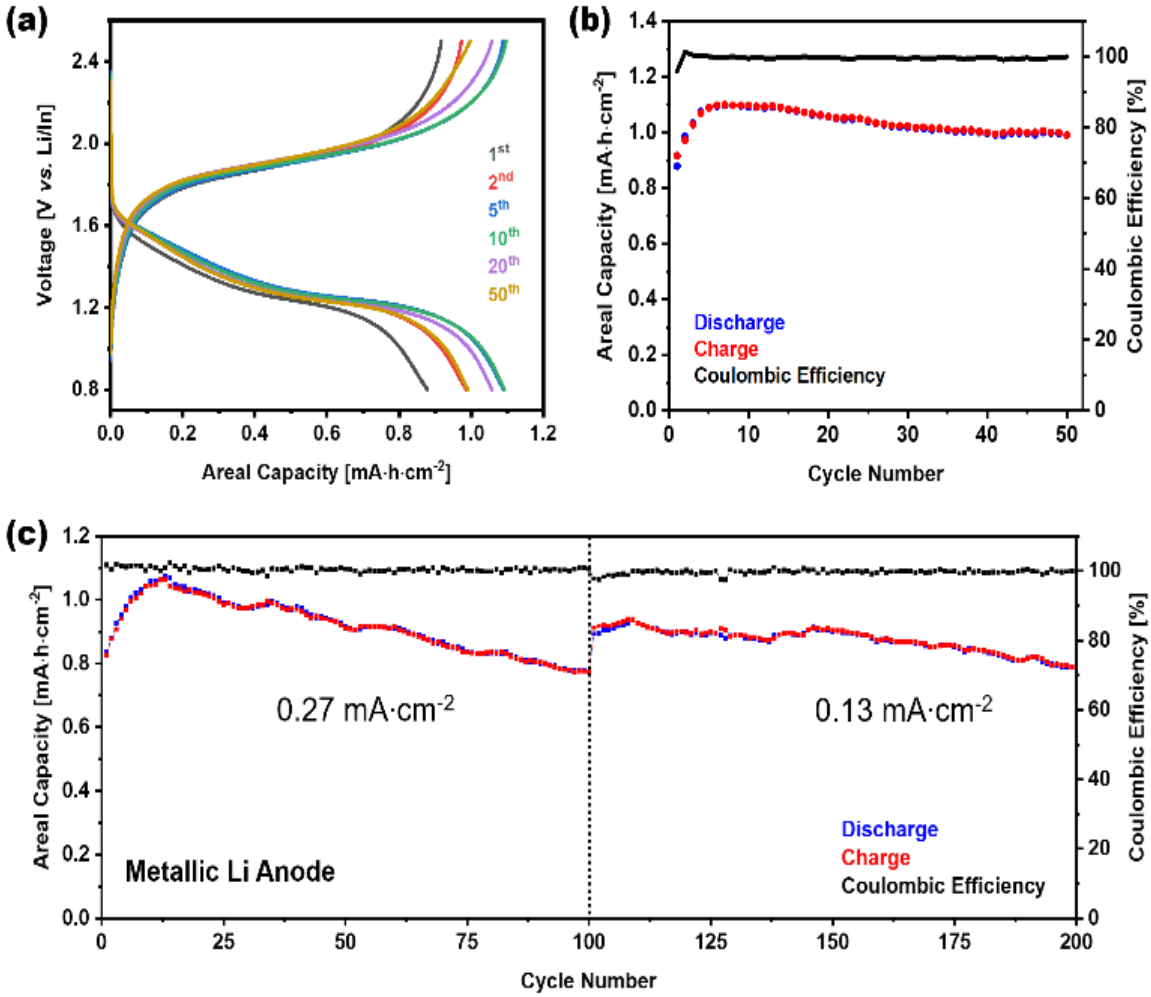


**Figure 3.7** Electrochemical performance of the solid-state Li-S/$VS_2$ battery. (a) Electrochemical profile and (b) long-term cycling of the solid-state cell at an active loading of 1.7 mg·cm$^{-2}$. Li/In alloy was utilized as the anode. (c) Long-term cycling of the solid-state Li-S/$VS_2$ battery (active loading: 1.9 mg·cm$^{-2}$) that utilized lithium metal as the anode. Current density was maintained at 0.27 mA·cm$^{-2}$ for the first 100 cycles and then adjusted to 0.13 mA·cm$^{-2}$ from the 101$^{st}$ cycle.

further boost the energy density at the cell level. The long-term cycling performance of the $S/VS_2|SE|Li$ cell is shown in **Figure 3.7 c**. The sulfur cathode delivered an initial discharge capacity of 0.82 $mA{\cdot}h{\cdot}cm^{-2}$ at an active material loading of 1.9 $mg{\cdot}cm^{-2}$ and exhibited good cycling performance at a current density of 0.27 $mA{\cdot}cm^{-2}$ (~C/5) for the first 100 cycles owing to the formation of a thin passivating layer of $Li_2S+Li_3P$ on Li metal.[85-86] The current density was halved to 0.13 $mA{\cdot}cm^{-2}$ for the following 100 cycles, where the cell displayed even better cycling performance with a stable capacity of 0.89 $mA{\cdot}h{\cdot}cm^{-2}$. In sharp contrast, the solid-state Li-S cell fabricated with Vulcan carbon as sulfur host exhibited a lower initial capacity of 0.74 $mA{\cdot}h{\cdot}cm^{-2}$, accompanied by a higher overpotential on discharge under the same cycling conditions (**Figure 3.8**). This further

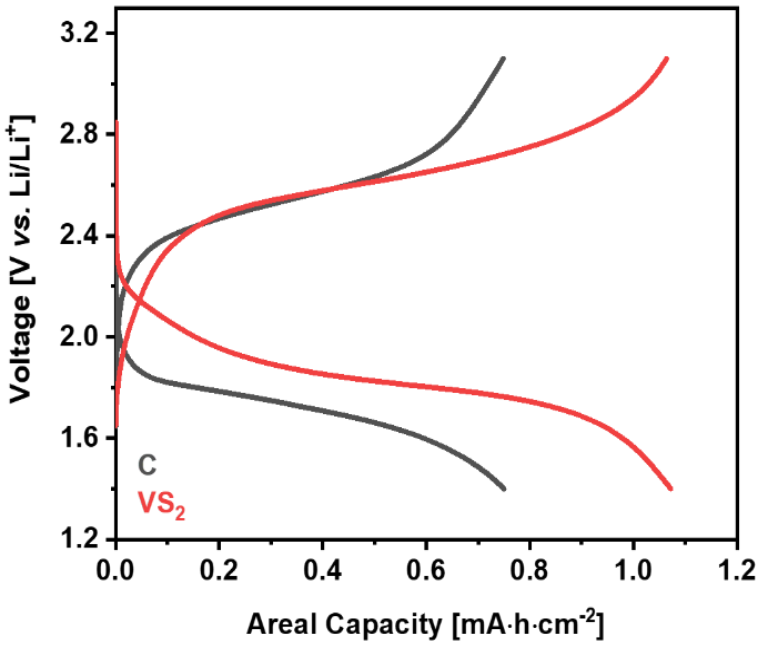


**Figure 3.8.** Electrochemical profile of the solid-state Li-S batteries fabricated with S/VC (black) and $S/VS_2$ (red) under a current density and sulfur loading of 0.27 $mA{\cdot}cm^{-2}$ and 0.6 $mg{\cdot}cm^{-2}$, respectively.

supports $VS_2$ acts more than just an electrical conduit for sulfur; it also provides additional capacity (233 $mA \cdot h \cdot g^{-1}$) in the electrochemical window of sulfur and serves as a lithium-ion vehicle. Both characteristics are irreplaceable by carbon materials.

Higher sulfur content in the composite was examined. However, further increasing

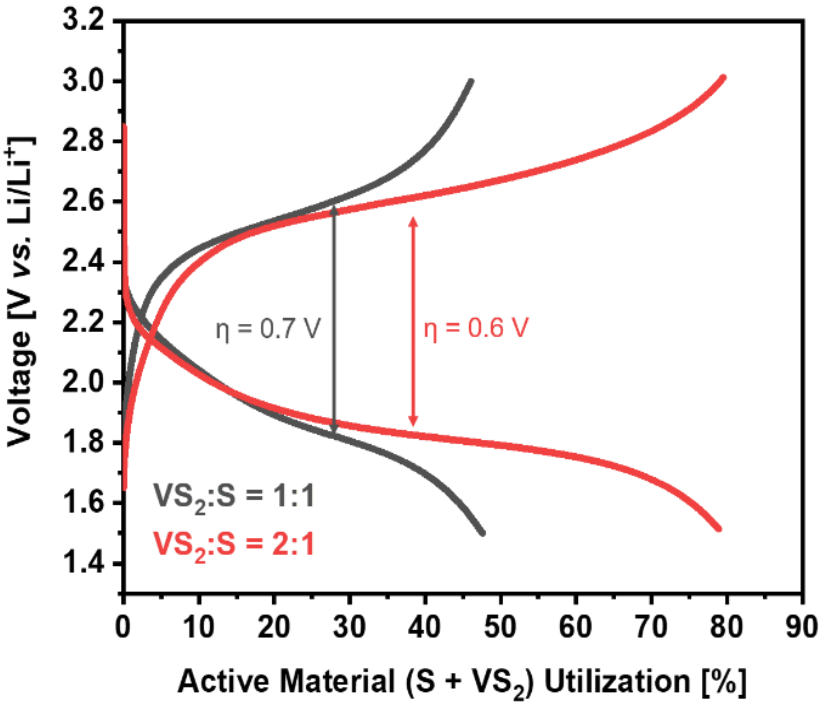


**Figure 3.9** Discharge/charge profile for the solid-state Li-S/$VS_2$ battery under weight ratio of $VS_2$ and sulfur in the cathode composite of 1:1 (black) and 2:1 (red). Capacity is normalized to their theoretical capacity achievable.

the sulfur content from 33 wt. % to 50 wt. % in the hybrid cathode may not only incur a higher cell polarization (0.6 V *vs.* 0.7 V) but also lower active material utilization (80 % *vs.* 47 %) (**Figure 3.9**). This can be attributed to the excessive insulating sulfur coating on the $VS_2$ materials that impedes the electronic conductivity of the cathode composite. Nonetheless, under the optimized $VS_2$:S ratio of 2:1, the solid-state Li-S/$VS_2$ cell

demonstrated excellent rate performance (**Figure 3.10)**. The cell exhibited a reversible capacity of 0.35 mA·h·cm$^{-2}$ at 0.5 mA·cm$^{-2}$ (C/2), and recovered back to 0.85 mA·h·cm$^{-2}$ when the current density reverted back to 0.2 mA·cm$^{-2}$ (C/5).

The electrochemical performance of cells with different cathode loadings was also examined. **Figure 3.11 a** presents the discharge/charge profile of the S/$VS_2$ cathode at an intermediate active material loading of 7.7 mg·cm$^{-2}$. The hybrid electrode offered an initial discharge capacity of 4 mA·h·cm$^{-2}$, which increased to 4.3 mA·h·cm$^{-2}$ in the fifth cycle at a current density of 0.12 mA·cm$^{-2}$. This corresponds to an active material utilization approaching 80 %. Moreover, an ultra-high loading (15.5 mg·cm$^{-2}$) cathode exhibited the highest reversible capacity up to 7.8 mA·h·cm$^{-2}$ at a current density of 0.12 mA·cm$^{-2}$ after the initial activation cycle (**Figure 3.11 b)**. The cells experienced a slight capacity decay, still delivering a reversible capacity of 5.2 mA·h·cm$^{-2}$ after 10 cycles, and this finding suggests binders are necessary at the cathode to accommodate the continuous volume expansion/contraction during cycling.[87] Nonetheless, this is amongst the highest areal

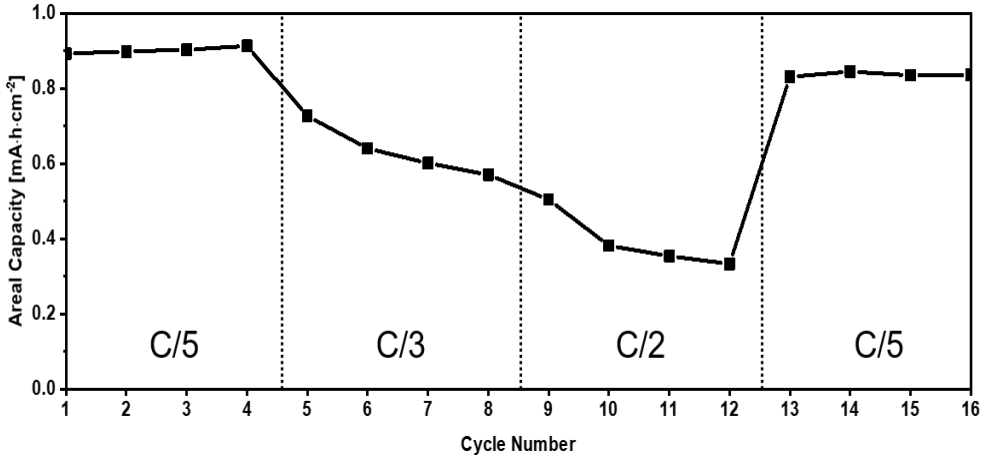


**Figure 3.10** Discharge capacities at different C-rates for the solid-state Li-S/$VS_2$ battery at an active material loading of 1.8 mg·cm$^{-2}$.

capacity reported for a solid state Li-S battery to our knowledge.[69,88] The capacity of each hybrid cathode at a different active material loading is compared in **Figure 3.11 c**. There is a gravimetric capacity penalty with an increasing loading owing to the higher polarization in the cell. These can be attributed to the lengthened electronic/ionic pathways in thick electrodes, a common phenomenon in liquid Li-S cells,[87] and can likely be

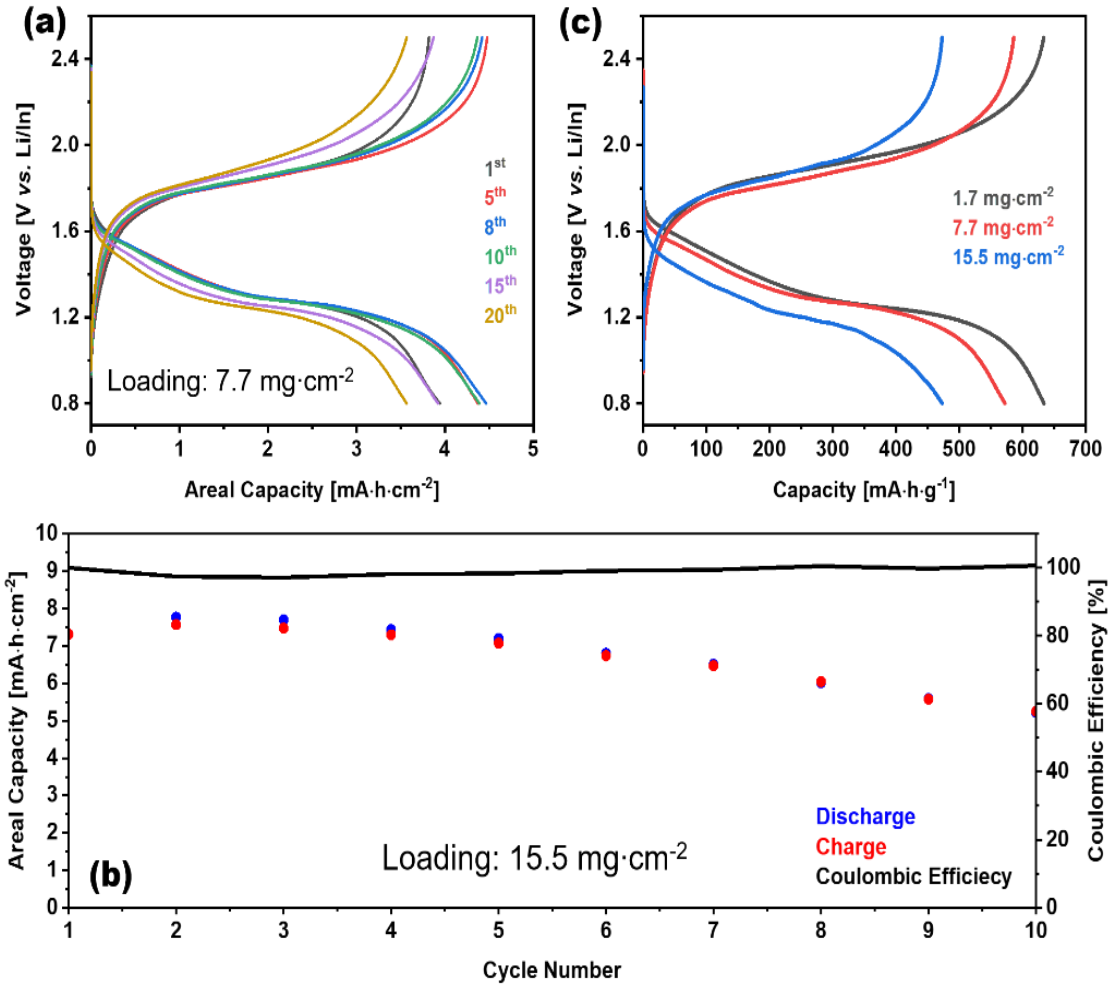


**Figure 3.11** Electrochemical profiles of solid-state Li-S batteries that utilized Li/In alloy as the anode at a cathode loading of (a) 7.7 mg·cm$^{-2}$ and (b) 15.5 mg·cm$^{-2}$. (c) The voltage profiles of cells with varied active material loadings as a function of gravimetric capacity.

improved by optimizing the cathode microstructure in future studies. The high areal capacity that is achieved is not only one of the highest reported to date in all-solid-state Li-S batteries, but is also comparable to some of the recent high sulfur loading studies in liquid Li-S batteries.[87,89] **Table 3.1** summarizes and compares the areal capacities of the recently reported all-solid-state Li-S cells, where the detailed mass ratio of the components in the cathode layer are provided (the mass of the current collectors and exterior package are omitted due to lack of information).

| **Positive Electrode (wt %)** | **Solid Electrolyte** | **Negative Electrode** | **Active material loading (mg)** | **Areal Capacity ($mA \cdot h \cdot cm^{-2}$)** | **Ref.** |
|---|---|---|---|---|---|
| S-[$Li_2S$+$P_2S_5$]-AC (50-40-10) | $Li_{10}GeP_2S_{12}$ | Li/In | 0.6 | 1.21 | [52] |
| [$Li_2S$+LiI]-VGCF-SE (50-10-40) | $Li_2S/P_2S_5$ | Li/In | 1.0 | 1.39 | [90] |
| S-CR-SE (9-21-20) | $Li_{10.05}Ge_{1.05}P_{1.95}S_{12}$ | Li/In | 0.9 | 0.86 | [91] |
| S-C-SE (20-10-70) | $Li_6PS_5Br$ | Li/In | 3 | 2.5 | [92] |
| [$Li_2S$+LiI]-VGCF-SE (75-10-15) | $Li_3PS_4$ | Li | 7.6 | 6.97 | [88] |
| S-C-SE (15-35-50) | $Li_{3.25}Ge_{0.25}P_{0.75}S_4$ | Li/Al | 0.75 | 1.7 | [93] |
| S-AB-SE (25-25-50) | $Li_{3.25}Ge_{0.25}P_{0.75}S_4$ | Li/In | 1.25 | 1.9 | [56] |
| S-$FeS_2$-C-SE (15-15-20-50) | LiI/$Li_3PS_4$ | Li | 6.6 | 3.55 | [69] |
| S-$VS_2$-SE (20-40-40) | $Li_3PS_4$ | Li/In | 12 | 7.8 | This work |

**Table 3.1** Selection of performance metrics of recent all solid-state Li-S batteries. The selection is limited due to the scarce number of papers reporting the areal capacity or the parameters needed for its calculation (active mass loading, electrode area). (Note: AB = acetylene black, AC = active carbon, VGCF = vaper grown carbon fiber, CR = carbon replica, and SE = solid state)

## 3.4 Conclusions

Our findings demonstrate that the combination of mixed ion/electron conductive transition metal sulfide and sulfur in an all-solid-state configuration is a promising strategy for the realization of next-generation solid-state batteries. The coating of an insulating sulfur layer on the $VS_2$ nanoplates results in a core-shell cathode architecture, and this morphology is well preserved owing to the low-energy physical blending process. Both factors minimize the surface contact between the electronically conductive component and $Li_3PS_4$, and hence reduce electrolyte decomposition on charge. The good performance relies on formation of a conversion-intercalation cathode that encompasses both lithium intercalation and metallic electronic conductivity. The $Li_xVS_2$ functions as a network that feeds both $Li^+/e^-$ to the active sulfur mass, while the $Li_3PS_4$ acts as the Li-ion conduit. The hybrid Li-S/$VS_2$ solid-state cell with a high active material loading of 15.5 $mg \cdot cm^{-2}$ and an areal capacity up to 7.8 $mA \cdot h \cdot cm^{-2}$, meets one of the major mandates for Li-S battery commercialization.[94] Benefiting from the collective electronic and ionic network afforded by the cathode architecture, these solid-state cells not only exhibit a very high Coulombic efficiency of 96 % in the first cycle but also achieve up to ~85 % sulfur utilization. This approach offers new promise for developing next-generation solid-state Li-S batteries.

# Chapter 4 Lithium sulfide-metal sulfide core-shell composite cathode for solid-state Li-S battery

## 4.1 Introduction

The encapsulation of $Li_2S$ particles by metal sulfide has been demonstrated to effectively accommodate $S/Li_2S$ volume change during cycling in Li-S batteries using both conventional liquid and polymer electrolyte.[95] Since the volume expansion also persists in all-solid-state Li-S batteries using inorganic solid electrolyte, it is worth exploring this encapsulation concept in this project. Herein, the lithium vanadium disulfide ($LiVS_2$) is coated on the surface of $Li_2S$ to form the core-shell composite, which is used as cathode active materials for all-solid-state Li-S batteries. $Li_2S$ is chosen as cathode active material because $Li_2S$ is already in the expanded state compared to sulfur, which prevents fracture of the encapsulation layer from volume expansion during cycling. The $LiVS_2$ encapsulation layer not only confines the $S/Li_2S$ volume change mostly within the shell, but also provides electronic conductivity using lower weight ratio compared with that in $VS_2$-S cathode from chapter 3. The confinement of $Li_2S$ in $LiVS_2$ encapsulation layer can support maintain the structure integrity and reduce the loss of active materials during cycling, which means a good capacity retention is expected after long-time charge and discharge process. With applying core-shell composite and high ionic solid electrolyte in cathode, the solid-state battery is expected to present a good electrochemical performance.

## 4.2 $Li_2S/LiVS_2$ core-shell composite prepared using commercial $Li_2S$

### 4.2.1 Experimental

*Synthesis of solid electrolyte*

$Li_{5.5}PS_{4.5}Cl_{1.5}$ is the solid-state electrolytes used in solid state Li-S battery. Lithium sulfide ($Li_2S$, Sigma-Aldrich, 99.98%), phosphorus pentasulfide ($P_2S_5$, Sigma-Aldrich, 99%), and lithium chloride (LiCl, Sigma-Aldrich, 99%) are precursors for the $Li_{5.5}PS_{4.5}Cl_{1.5}$ synthesis. The stoichiometric amounts of three precursors (total weight ~500 mg) were mixed in a mortar for ten minutes in an argon filled glovebox and then ball milled with 150 balls in a sealed zirconia jar using a high energy ball-milling planetary. The milling speed and duration was kept at 380 rpm and 12h, respectively. Afterwards, powders were collected from the jar and pelletized in a 10 mm die. The pellet was placed in a glassy carbon capped crucible and vacuum-sealed in a quartz tube, and heat treated at 550 ºC for 12 hours. After heat-treatment, the $Li_{5.5}PS_{4.5}Cl_{1.5}$ was achieved. All quartz tubes were preheated for two days at 100 ºC under vacuum to remove traces of water.

*Synthesis of $Li_2S/VS_2$ composite and cathode*

Vanadium sulfide encapsulated lithium sulfide ($Li_2S/VS_2$) particles were prepared by the in-situ reaction of lithium sulfide ($Li_2S$) with vanadium chloride ($VCl_4$): $2Li_2S + VCl_4 = VS_2 + 4LiCl$.[96] Commercial bulk $Li_2S$ (named as b-$Li_2S$) particles were firstly ball-milled for 2 h. Then, 230 mg of $Li_2S$ (5 mmol) was added into the solution of 0.7 mmoL $VCl_4$ (99.9%, Sigma-Aldrich) in tetrahydrofuran (THF) (20 ml) to convert the $Li_2S$ on the surface into $VS_2$. The solution immediately turned to dark purple. After stirring at room

temperature for 12h, the resulting dark solids were centrifugated and washed with THF to remove the side products. Finally, b-$Li_2S/VS_2$ particles were obtained after heating the above product at 400 ℃ for 6 h. The cathode composite material was prepared by a physical blend of the b-$Li_2S/VS_2$ composite material and SSE with a ratio of 5:5 in a glovebox.

### 4.2.2 Physical characterizations

A series of physical characterizations were carried on obtained core shell particles. The XRD pattern of core shell composite is shown in **Figure 4.1**, which confirmed a dominant phase of $Li_2S$ and existence of $LiVS_2$. However, the $VS_2$ should be found rather than $LiVS_2$ based on the reaction mechanism in experimental. The existence of $LiVS_2$ proved that there were some further reactions on the synthesized $VS_2$. A reasonable assumption is that the extra $Li_2S$ reacted with $VS_2$ to form $LiVS_2$. To examine the assumption, $Li_2S$ and $VS_2$ were directly mixed with a ratio of 2:1 in THF 12h to check any possible reactions. In **Figure 4.2**, the THF solution contained mixture of $Li_2S$ and $VS_2$ in

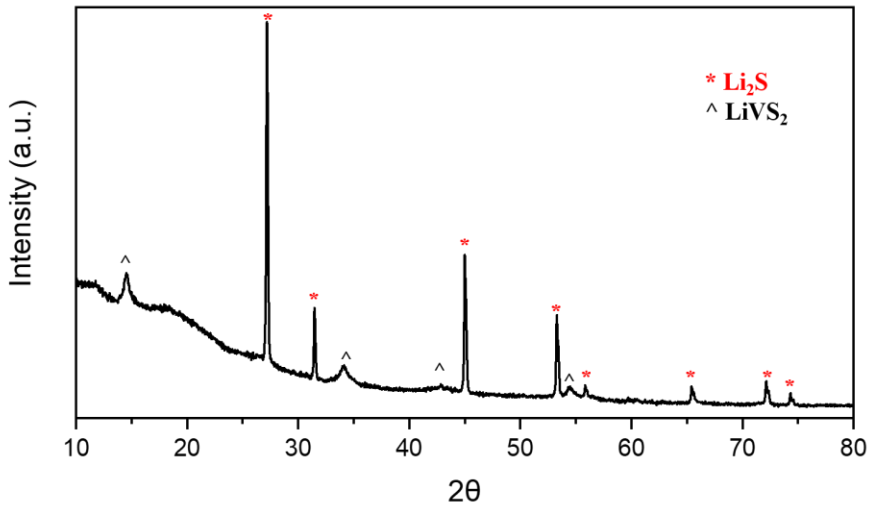


**Figure 4.1** The XRD pattern of b-$Li_2S/LiVS_2$ composite

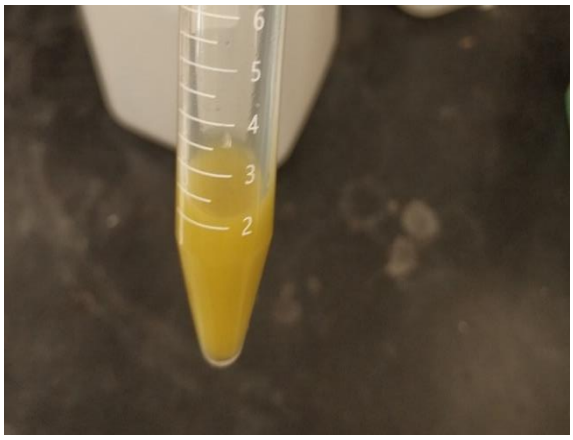


**Figure 4.2** The image of mixing $Li_2S$ and $VS_2$ in THF.

centrifugation tube showed a yellow color. The yellow color may correspond to color of polysulfides and proved the occurrence of some reactions. After centrifugation, the powders were collected and examined with XRD, as shown in **Figure 4.3**. The clear peaks corresponding to $Li_2S$ and $LiVS_2$ demonstrated the assumption that $Li_2S$ reacted with $VS_2$ to form $LiVS_2$ in THF solution. In this reaction, $VS_2$ is reduced to form with $LiVS_2$ while $Li_2S$ is believed to have been oxidized to polysulfide (*e.g.* $Li_2S_2$). However, the exact speciation of that polysulfide is yet to be determined and will be subject to future study.

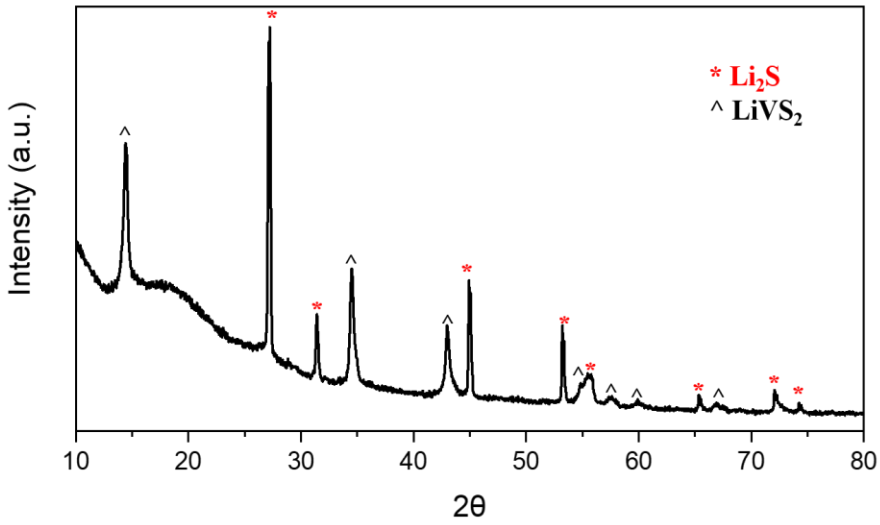


**Figure 4.3** XRD pattern of the mixture of $Li_2S$ and $VS_2$ in THF

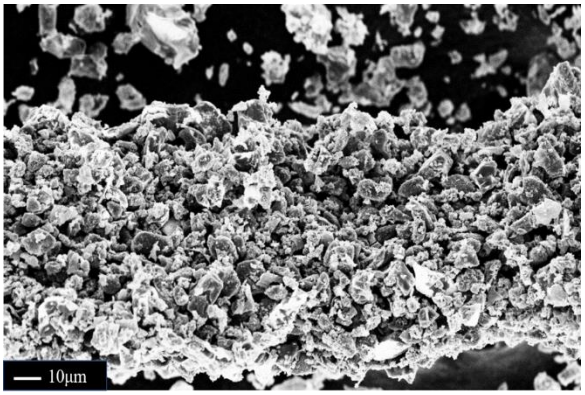


**Figure 4.4** The SEM image of b-$Li_2S/LiVS_2$

Though $LiVS_2$ is not expected before the synthesis of core shell composite, the $LiVS_2$ encapsulation layer is possibly beneficial since $Li^+$ intercalation of metallic $VS_2$ may provide better ionic pathway and improve the performance of solid-state battery. The SEM image in **Figure 4.4** exhibited the b-$Li_2S/LiVS_2$ composite, which consisted of large particles with rough surface.

The XRD pattern of the synthesized $Li_{5.5}PS_{4.5}Cl_{1.5}$ is shown in **Figure 4.5 a**. It confirmed a dominant phase of $Li_{5.5}PS_{4.5}Cl_{1.5}$. The peak of $Li_{5.5}PS_{4.5}Cl_{1.5}$ corresponded

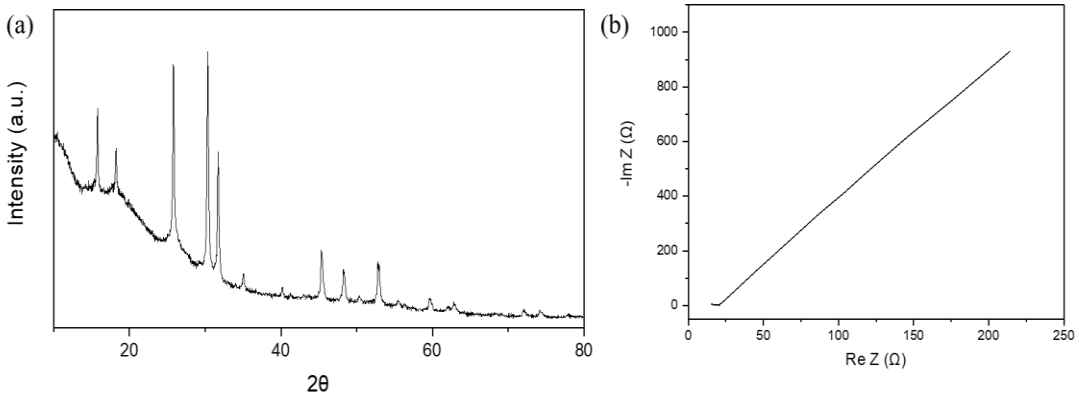


**Figure 4.5** (a) XRD pattern of the synthesized $Li_{5.5}PS_{4.5}Cl_{1.5}$ (b) Nyquist plot of the $Li_{5.5}PS_{4.5}Cl_{1.5}$ electrolyte measured at 25 ºC. The ionic conductivity was determined to be 7.1 $mS \cdot cm^{-1}$.

well as reported in previous work of our group.[97] The ionic conductivity of $Li_{5.5}PS_{4.5}Cl_{1.5}$ was determined to be 7.1 mS·cm$^{-1}$ at 25 ºC by EIS measurements, as shown in **Figure 4.5 b**.

### 4.2.3 Electrochemical measurements and results

The b-$Li_2S$/$LiVS_2$ core-shell composite was successfully synthesized and used as cathode active material in a solid-state cell. The electrochemical performance of the solid-state Li-S battery was carried out using a home-designed cell. In this solid-state cell, b-$Li_2S$/$LiVS_2$/$Li_{5.5}PS_{4.5}Cl_{1.5}$ composite served as the cathode and Li-In alloy was used as corresponding anode. Approximate 70 mg of $Li_{5.5}PS_{4.5}Cl_{1.5}$ worked as a separator. Galvanostatic cycling was performed in the voltage range of 0.9-2.6 V *vs.* Li-In alloy. The theoretical capacity of the $Li_2S$/$LiVS_2$ cathode is 789 mA·h·g$^{-1}$ at a $Li_2S$:$LiVS_2$ weight ratio of 3:2.

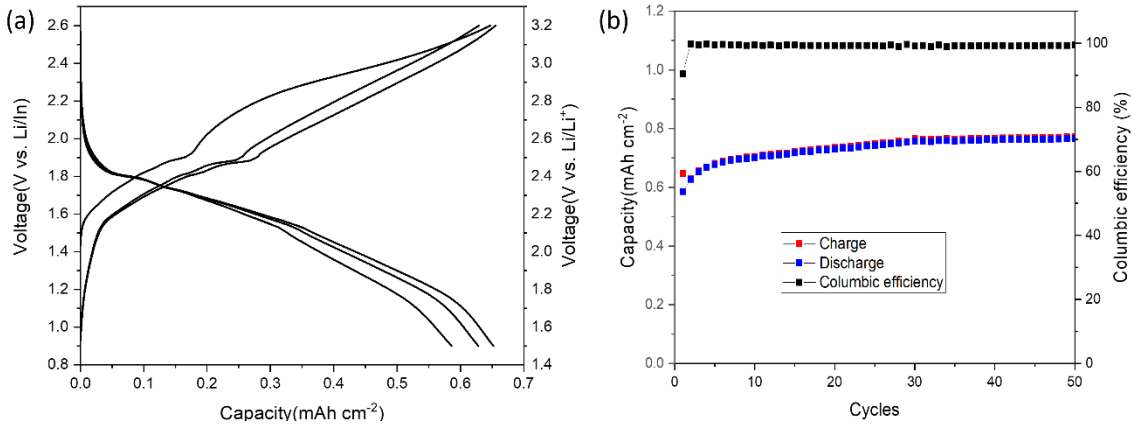


**Figure 4.6** (a) The galvanostatic cycling profiles of b-$Li_2S$/$LiVS_2$ composite cathode and (b) The long-term cycling of the b-$Li_2S$/$LiVS_2$ composite cathode at an active material loading of 1.4 mg·cm$^{-2}$.

The galvanostatic cycling profile of solid-state Li-S battery using b-$Li_2S/LiVS_2$ composite indicated the core shell composite was electrochemically active during the voltage window (0.9-2.6 V), as shown in **Figure 4.6 a**. The initial areal capacity of the cathode was ~ 0.6 $mA{\cdot}h{\cdot}cm^{-2}$ at C/10, corresponding to a 55% total utilization of active materials. When $LiVS_2$ was assumed to reach its theoretical capacity and its contribution was removed from total capacity, the initial discharge capacity of $Li_2S$ were 570 $mA{\cdot}h\ g^{-1}$ based on the calculation. In terms of long-term cycling (**Figure 4.6 b**), the b-$Li_2S/LiVS_2$ composite cathode did not decay and remained 70% of total utilization over 50 cycles at C/10, presenting a good stability.

In summary, the solid-state cell using b-$Li_2S/LiVS_2$ composite cathode exhibited a good electrochemical performance. Compared with the $S/VS_2$ cathode (slow decay after 20 cycles), the b-$Li_2S/LiVS_2$ cathode presented a better cycle stability. There is still a potential to further improve the performance of the cell if $Li_2S$ with smaller particle size is used in synthesis of core-shell composite. In the next section (Section 4.3), the $Li_2S/LiVS_2$ composite synthesized using nanosized $Li_2S$ particle will be introduced.

# 4.3 $Li_2S/LiVS_2$ core-shell composite prepared using nanosized $Li_2S$

## 4.3.1 Experimental

### *Synthesis of nanosized $Li_2S$*

In this section, three different syntheses of $Li_2S$ have been attempted. In the first one, lithium triethylborohydride ($LiEt_3BH$) and sulfur were used to produce $Li_2S$. In brief, 160 mg sulfur was added in 1.19 ml $LiEt_3BH$ in THF to react for 10 mins with the stirred bar

in a flask. After that, the flask was sealed and taken out of glovebox to connect with a vacuum pump. All the solvent inside was removed overnight. Then, the flask was transferred back into glove box. Chemicals in flask were collected into a centrifugation tube and washed with THF for 3-4 times. The collected solid samples were dried in the Büchi vacuum oven under 150 degrees for 12h.[98]

In the second one, lithium sulfate monohydrate ($Li_2SO_4 \cdot H_2O$) and Ketjen Black were used to synthesize $Li_2S$. In order to reduce the particle size and to ensure sufficient mixing, $Li_2SO_4 \cdot H_2O$ and Ketjen Black were ball milled for 60 h at 400 rpm with 10 min interval in a zirconia lined grinding beaker with 1 mm sized zirconia balls within a dispersion of ethanol. Subsequent carbothermal reduction of lithium sulfate monohydrate/Ketjen Black powder, with 66wt% $Li_2SO_4 \cdot H_2O$, was executed at 820 °C for 3 h with an argon gas flow in a 40 mm diameter tube furnace. After the heat treatment, the sample was directly transferred into an argon filled glove box.[99]

In the third one, lithium naphthalenide (LiNAP) and sulfur were used to synthesize $Li_2S$. First, 1.24 ml naphthalene was dissolved in 20 ml THF to from a uniform solution with the stirred bar in a vial. After that, 70 mg of lithium metal was added into above solution to form lithium naphthalenide, which took 1-2 day to react completely. Then, 160 mg sulfur was added into lithium naphthalenide by several times to make sure the vial was not too hot. After 3 days reaction, the material in the vial were transfered into a centrifugation tube and washed with DME/THF for 3-4 times. The collected solid samples were dried in the Büchi vacuum oven under 150 degrees for 12h.[100]

The solid-state electrolyte used in this part and the synthesis of $Li_2S/LiVS_2$ composite are same as section **4.2.1**. The only difference is that the nanosized $Li_2S$ was used as the

active material.

### 4.3.2 Physical characterizations

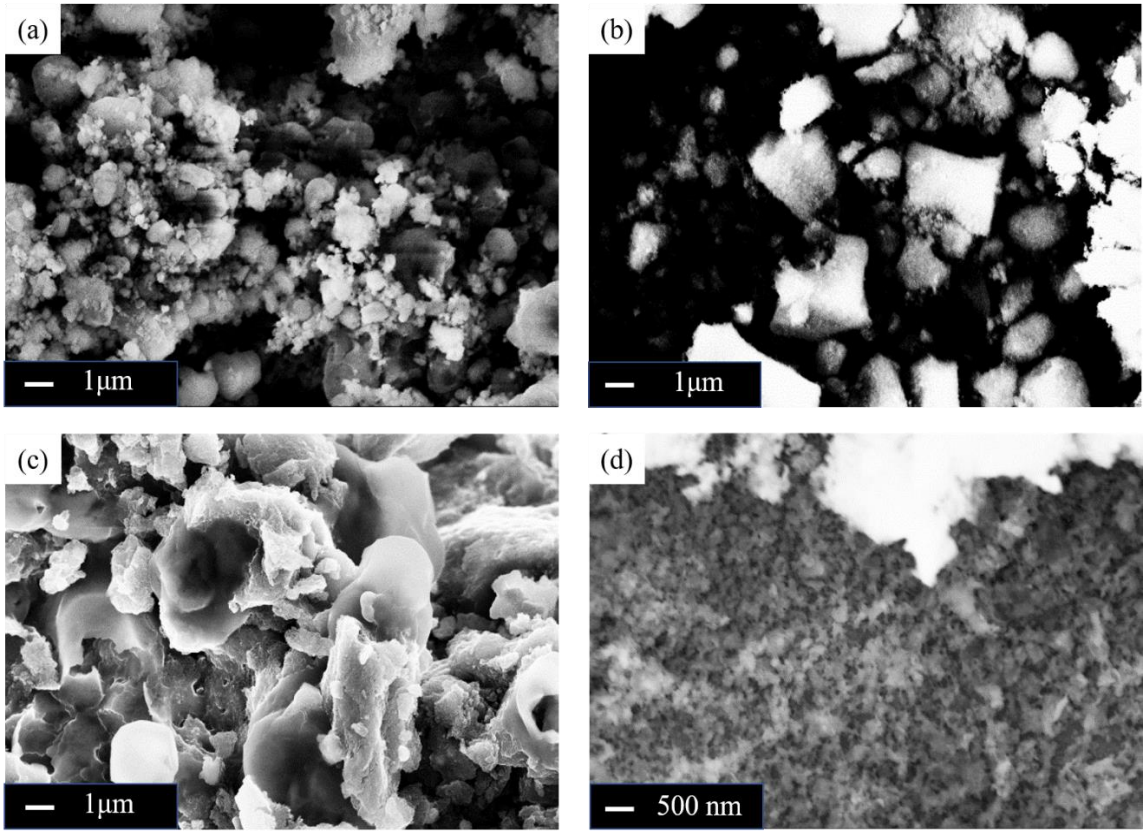


**Figure 4.7** The SEM images of (a) commercial $Li_2S$, (b) $Li_2S$ synthesized from $LiEt_3BH$ precursor, (c) $Li_2S$ synthesized from $Li_2SO_4 \cdot H_2O$ precursor, and (d) $Li_2S$ synthesized from LiNAP precursor.

To achieve smaller particle size of $Li_2S$, homemade $Li_2S$ was synthesized based on three methods introduced in experimental. In the SEM images of four different $Li_2S$ particles (**Figure 4.7**), the $Li_2S$ synthesized from $LiEt_3BH$ (**Figure 4.7 b**) had similar particle size as commercial one (**Figure 4.7 a**), approximately 2-3 micrometers; The $Li_2S$ synthesized from $Li_2SO_4 \cdot H_2O$ exhibited even larger particle size, around 5 micrometers;

The $Li_2S$ synthesized from LiNAP precursor showed smallest particle size, approximately 200 nm. Therefore, the nanosized $Li_2S$ (named as n-$Li_2S$) synthesized from LiNAP was used as new precursor for $Li_2S/LiVS_2$ composite synthesis. The XRD pattern of nanosized

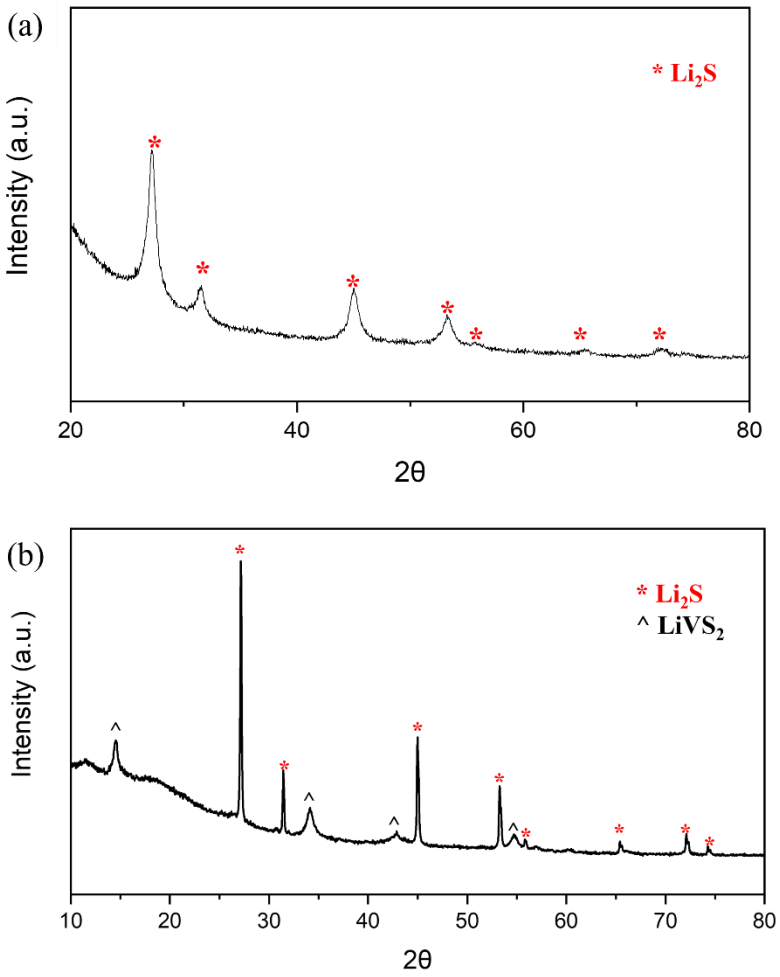


**Figure 4.8** XRD pattern of (a) nanosized $Li_2S$ and (b) n-$Li_2S/LiVS_2$ composite.

$Li_2S$ is shown in **Figure 4.8 a**. After synthesis of n-$Li_2S/LiVS_2$ core-shell composite, the XRD was conducted on the collected powder, as shown in **Figure 4.8 b**. The peaks of both $Li_2S$ and $LiVS_2$ are clear and obvious, which demonstrated a success of synthesis. The peaks of $Li_2S$ in core-shell composite turned to be sharper because the 400 ℃ heat treatment crystallized the particles.

### 4.3.3 Electrochemical measurements and results

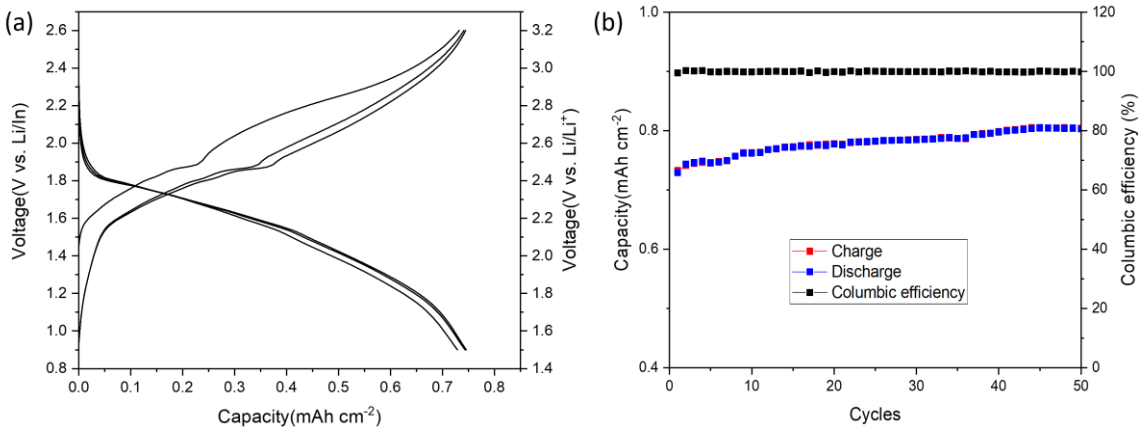


**Figure 4.9** (a) The galvanostatic cycling of n-$Li_2S$/$LiVS_2$ composite cathode and (b) long-term cycling of n-$Li_2S$/$LiVS_2$ composite cathode at an active material loading of 1.4 mg·$cm^{-2}$.

The n-$Li_2S$/$LiVS_2$ core-shell composite was successfully synthesized. In combination of $Li_{5.5}PS_{4.5}Cl_{1.5}$, the n-$Li_2S$/$LiVS_2$/$Li_{5.5}PS_{4.5}Cl_{1.5}$ composite served as cathode for solid-state Li-S cell. The galvanostatic cycling profile of n-$Li_2S$-$LiVS_2$ composite (**Figure 4.9 a**) exhibited an initial areal capacity of 0.72 mA·h·$cm^{-2}$ at C/10 within the voltage window (0.9-2.6 V *vs.* Li-In), which corresponded to a 65% total utilization. After removing contribution from $LiVS_2$, the initial discharge capacity of $Li_2S$ were 710 mA·h·$g^{-1}$ based on calculation. The principle of calculation for active material is introduced in page 46, the $LiVS_2$ was assumed to reach its theoretical capacity and its contribution was removed from total capacity. The rest capacity can be considered as contribution of $Li_2S$. In terms of long-term cycling (**Figure 4.9 b**), the nano $Li_2S$-$LiVS_2$ composite remained 75% of total utilization over 50 cycles at C/10. It is obvious that the n-$Li_2S$/$LiVS_2$ composite presented

better performance than b-$Li_2S/LiVS_2$ composite, no matter on capacity retention or the cycle stability. In addition, the n-$Li_2S/LiVS_2$ composite also showed better stability than $S/VS_2$ composite in chapter 3, which is expected.

A relatively high loading cathode (4 mg·cm$^{-2}$) using n-$Li_2S/LiVS_2$ composite (**Figure**

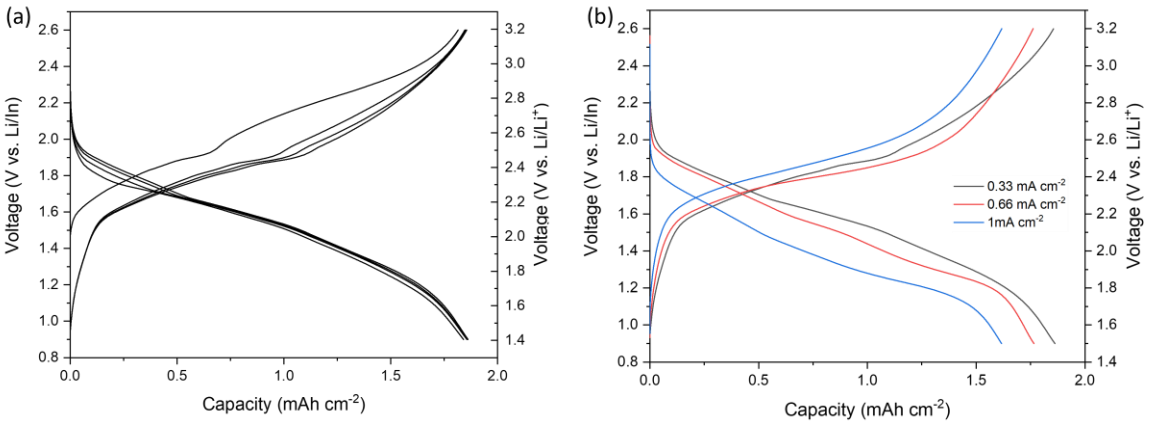


**Figure 4.10** (a) The galvanostatic cycling profile of n-$Li_2S/LiVS_2$ composite cathode and (b) Cycling profile at different C-rates for the solid-state n-$Li_2S/LiVS_2$ battery at an active material loading of 4 mg·cm$^{-2}$.

**4.10 a**) exhibited a capacity of 1.85 mA·h·cm$^{-2}$ at C/10 within voltage window (0.9-2.6 V vs Li-In), which corresponds to a 58% total utilization. The utilization decreased because the loading of active material increased, along with higher current density. The cell exhibited a reversible capacity of 1.85 mA·h·cm$^{-2}$ at 0.33 mA·cm$^{-2}$ (C/10, cycle 4),1.76 mA·h·cm$^{-2}$ at 0.66 mA·cm$^{-2}$ (C/5, cycle 30), and 1.61 mA·h·cm$^{-2}$ at 1 mA·cm$^{-2}$ (C/3, cycle 140), respectively (**Figure 4.10 b**). In addition, it maintained an excellent capacity of 1.75 mA·h·cm$^{-2}$ after 100 cycles at 0.66 mA·cm$^{-2}$, which is shown in **Figure 4.11**. Though the overpotential increased and the capacity dropped when applying higher current density on the cell, this n-$Li_2S/LiVS_2$ composite cathode still exhibited a good battery performance

and excellent cycle stability.

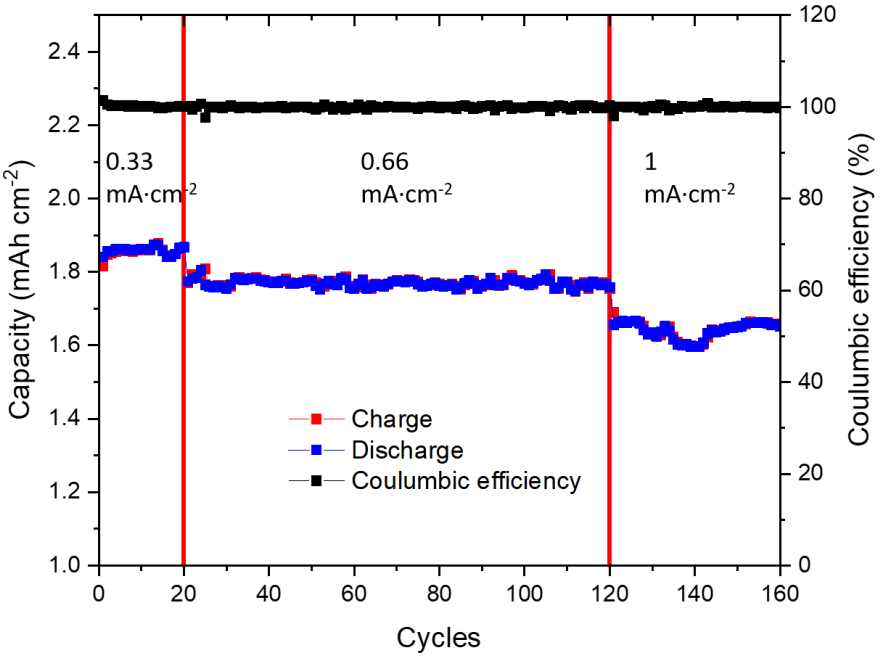


**Figure 4.11** The long-term cycling of the solid-state n-$Li_2S$/$LiVS_2$ battery (active loading: 4 mg·$cm^{-2}$) when current density was set at 0.33 mA·$cm^{-2}$ (1-20 cycles), 0.66 mA·$cm^{-2}$ (21-120 cycles) and 1 mA·$cm^{-2}$ (121-160 cycles), respectively.

## 4.4 Conclusion

In this project, the use of $Li_2S$/$LiVS_2$ core shell composite to construct cathodes in solid-state cell was explored. The coating of a $LiVS_2$ layer on the surface of $Li_2S$ particles results in a core-shell architecture, and this morphology can be well preserved under the physical blending process. $LiVS_2$ fed $e^-$ to the $Li_2S$ and the $Li_{5.5}PS_{4.5}Cl_{1.5}$ acted as the Li-ion conduit. It is expected that the cathode architecture provided a collective electronic and ionic network, which is a necessary for the good battery performance. There were two

kinds of composite synthesized and tested here, the n-$Li_2S/LiVS_2$ composite demonstrated superior capacity retention than b-$Li_2S/LiVS_2$ composite, which not only exhibited a good coulombic efficiency but also achieved ~75 % total utilization. The cycle stability of n-$Li_2S/LiVS_2$ core-shell composite is better than that of the S-$VS_2$ composite synthesized by melt diffusion. The better cycle stability resulted from the core-shell architecture, in which $LiVS_2$ encapsulation layer confine the volume change of $Li_2S$ inside the shell, reducing the loss of active materials isolated from ionic and electronic network during cycling. In future, more experiments will be conducted on testing cycle stability of high-loading cell with high current density. In general, the $Li_2S/LiVS_2$ core shell composite in an all-solid-state configuration is an interesting direction for next-generation batteries.

# Chapter 5 Summary and future perspectives

The work presented in this thesis focuses on the positive electrode materials for solid-state Li-S battery. Currently, in order to develop a solid-state Li-S cell to operate with high specific capacity, rate capability, and prolonged cycle performance, the positive electrode is still the most challenging and hindered part. Maintaining a good balance between electronic and ionic conductivity in cathode is considered to be an important factor and is the main problem to be solved in this thesis.

In the first part of the thesis, a metallic vanadium disulfide with ionic pathway was synthesized and applied as a sulfur host for solid state Li-S cell. It is bifunctional in providing electronic conductivity and extra capacity. The *ex-situ* XRD analysis confirmed the co-existence of $Li_xVS_2$ and $Li_2S$, which means electrochemical mechanism of the Li-S/$VS_2$ battery follows a simultaneous conversion/(de)lithiation process. However, whether $VS_2$ can serve as a Li-ion delivery vehicle for sulfur (*i.e.*, $Li_xVS_2 + S \leftrightarrow Li_2S + VS_2$) or not was not directly proved in this project, which will be the subject of future studies. With the aim of improving cycle stability of high-loading cells, the development of cathode where expansion/contraction can be controlled will be explored in future work.

In the second part, the use of $Li_2S/LiVS_2$ core-shell composite in solid-state $Li_2S$ cathode was explored. $Li_2S/LiVS_2$ composite synthesized from nanosized $Li_2S$ demonstrated superior capacity retention than that synthesized from bulk $Li_2S$. $Li_2S/LiVS_2$ core-shell composite has similar electrochemical mechanism as S/$VS_2$ composite. The addition role of $LiVS_2$ in supporting lithium-ion transference from $Li_2S$ is also explored. On the other hand, since $Li_2S/LiVS_2$ composite showed the potential to maintain the consistence of cathode structure under high current density. Therefore, long cycles of high-

loading $Li_2S/LiVS_2$ solid-state cells at high current density (such as C/2) will be main research aim in future. In addition, in order to commercialize solid-state Li-S battery, the anode and electrolyte need to be improved as well.

# References


[1] J. B. Goodenough, Y. Kim, *Chem. Mater.* **2010**, *22*, 587.

[2] J. B. Goodenough, K.S. Park, *J. Am. Chem. Soc.* **2013**, *135*, 1167.

[3] J. M. Tarascon, M. Armand, *Nature.* **2001**, *414*, 359.

[4] K. Mizushima, P. C. Jones, P. J. Wiseman, J. B. Goodenough, *Mater. Res. Bull.* **1980**, *15*, 783.

[5] P. G. Bruce, S. A. Freunberger, L. J. Hardwick, J. M. Tarascon, *Nat. Mater.* **2012**, *11*, 19.

[6] S. Evers, L. F. Nazar, *Acc. Chem. Res.* **2012**, *46*, 1135.

[7] A. Manthiram, Y. S. Su, *Chem. Rev.* **2014,** *114*, 11751.

[8] T. Knoxville, J. Dean, *Lange's handbook of chemistry*. McGraw-Hill, New York, United States of America, **1999,** 279.

[9] X.B. Cheng, Q. Zhang, *J. Electrochem. Soc.* **2018**, 165, A6058.

[10] Y. V. Mikhaylik, J. R. Akridge, *J. Electrochem. Soc.* **2004**., *151*, A1969.

[11] M. Wild, L. O'Neill, T. Zhang, R. Purkayastha, G. Minton, M. Marinescu, G. J. Offer, *Energy Environ. Sci.* **2015**, *8*, 3477.

[12] X. Ji, K. T. Lee, L. F. Nazar, *Nat. Mat.* **2009**, *8*, 500.

[13] G. Zheng, Q. Zhang, J. J. Cha, Y. Cui, *Nano Lett.* **2013**, *13*, 1265.

[14] M. Liu, F. Ye, W. Li, H. Li, Y. Zhang, *Nano Res.* **2016,** *9*, 94.

[15] H. Wang, Y. Yang, Y. Liang, J.T. Robinson, Y. Li, A. Jackson, Y. Cui, H. Dai, *Nano Lett.* **2011**, *11*, 2644.

[16] L. Ji, M. Rao, H. Zheng, L. Zhang, Y. Li, W. Duan, J. Guo, E.J. Cairns, Y. Zhang, *J. Am. Chem. Soc.* **2011**, *133*, 18522.

[17] X. Liu, J. Huang, L. Mai, *Adv. Mat.* **2017**, *29*, 1601759.

[18] A. Gorkovenko, *et al. United States Patent, US6210831.* Patented April 4, **2001**.

[19] M. S. Song, S. C. Han, H. S. Kim, J. H. Kim, K. T. Kim, Y. M. Kang, H. J. Ahn, S.X. Dou, J. Y. Lee, *J. Electrochem. Soc.* **2004**, *151*, A791.

[20] Tang, Hao, et al. *J. Alloys Compd.* **2015,** *650*, 351.

[21] S. Evers, T. Yim, L. F. Nazar, *J. Phys. Chem. C.* **2012,** *116*, 19653.

[22] X. Chen, H. Peng, R. Zhang, T. Hou, J. Huang, B. Li, Q. Zhang, *ACS Energy Lett.* **2017**, *2*, 795801

[23] X. Zhu, W.Zhao, Y. Song, Q. Li, F. Ding, J. Sun, L. Zhang, Z. Liu, *Adv. Energy Mat.* **2018**, *8*, 1800201.

[24] L. Fan, M. Li, X. Li, W. Xiao, Z. Chen, J. Lu, *Joule*, **2019**, *3*, 361.

[25] M. Whittingham, *Chem. Rev.* **2004**, *104*, 4271.

[26] J. Fergus, *J. Power Sources*. **2010,** *195*, 939.

[27] C. Vincent, *Solid State Ionics*. **2000**, *134*, 159.

[28] J. Liu, *et al. Nano Energy*. **2017**, *31*, 478.

[29] M. Agostini, Y. Aihara, T. Yamada, *Solid State Ionics.* **2013**, *244*, 48.

[30] Y.X. Xiang, G. Zheng, G. Zhong, *Solid State Ionics.* **2018**, *318*, 19.

[31] R.A. Sharma, *J. Electrochem. Soc.* **1972**,*119*, 1439.

[32] T. Takeuchi, K. Hiroyuki, N. Koji, T. Mitsuharu, T. Kuniaki, *J. Electrochem. Soc.* **2010**, *157*, A1196.

[33] A. Manthiram, X. Yu, S. Wang, *Nat. Rev. Mater.* **2017**, *2*, 16103.

[34] T. Hakari, M. Nagao, A. Hayashi, M. Tatsumisago, *J. Power Sources.* **2015**, *293*, 721.

[35] T. Hakari, *et al. Chem. Mater.* **2017**, *29*, 4768.

[36] Y. Zhu, X. He, Y. Mo, *ACS Appl. Mater. Interfaces.* **2015**, *7*, 23685.

[37] Y, T. Seino, T. Ota, A. Hayashi, M. Tatsumisago, *Energy Environ. Sci.* **2014**, 7, 627.

[38] K. Minami, A. Hayashi, M. Tatsumisago, *J Non Cryst Solids*. **2010**, *356*, 44.

[39] P. Adeli, J. D Bazak, K. H. Park, I. Kochetkov, A. Huq, G. R. Goward, L. F. Nazar, *Angew. Chem. Int. Ed.* **2019**, *58*, 8681.

[40] C. Cao, Z. B. Li, X. L. Wang, X. B. Zhao, W. Q. Han, *Front. energy res.* **2014**, *2*, 25.

[41] M. Nagao, A. Hayashi, M. Tatsumisago, *Electrochim. Acta.* **2011,** *56*, 6055.

[42] H. Nagata, Y. Chikusa, *Energy Technol*. **2015,** *4*, 484.

[43] X. Li, *et al. Adv. Mater.* **2019**, *31*, 1808100.

[44] M. Nagao, A. Hayashi, M. Tatsumisago, *J. Mater. Chem.* **2012**, *22*, 10015.

[45] S. Choi, W.T. Nichols, *et al. Ceram. Int.* **2018**, *44*, 7450.

[46] X. Ruochen, L. Sufu, *et al. ACS Energy Letters.* **2019**, *4*, 1073.

[47] D. Herbert, J. Ulam, *United States Patent, US3043896A.* Patented July 10, **1962**.

[48] Georgia State University, http://hyperphysics. phyastr.gsu.edu /hbase/quantum/ bragg. August 17, **2021**.

[49] C. Sun, L. Shi, C. Fan, X. Fu, Z. Ren, G. Qian, Z. Wang, *RSC Advances.* **2015**, *3*, 127

[50] Pveducation, https://pveducation.org/ pvcdrom/ characterisation / four-point-probe resistivity. August 17, **2021**.

[51] D. Houtarde, *Master's thesis, University of Waterloo*. **2015**.

[52] H. Nagata, Y. Chikusa, *J. Power Sources.* **2014**, *264*, 206.

[53] E. Umeshbabu, B. Zheng, Y. Yang, *Electrochem. Energy Rev.* **2019**, *2*, 199.

[54] T. Yamada, S. Ito, R. Omoda, T. Watanabe, Y. Aihara, M. Agostini, U. Ulissi, J. Hassoun, B. Scrosati, *J. Electrochem. Soc.* **2015**, *162*, A646.

[55] D. Lei, K. Shi, H. Ye, Z, Wan, Y. Wang, L. Shen, B. Li, Q.-H. Yang, F. Kang, Y.-B. He, *Adv. Funct. Mater.* **2018**, *28*, 1707570.

[56] J. Lau, R. H. deBlock, D. M. Butts, D. S. Ashby, C. S. Choi, B. S. Dunn, *Adv. Energy Mater*. **2018**, *8*, 1800933.

[57] P. Bonnick, K. Niitani, M. Nose, K. Suto, T. S. Arthur, J. Muldoon, *J. Mater. Chem. A.* **2019**, *7*, 24173.

[58] W. Zhang, T. Leichtweiß, S. P. Culver, R. Koerver, D. Das, D. A. Weber, W. G. Zeier, J. Janek, *ACS Appl. Mater. Interfaces.* **2017**, *9*, 35888.

[59] F. Han, Y. Zhu, X. He, Y. Mo, C. Wang, *Adv. Energy Mater.* **2016**, *6*, 1501590.

[60] J. Yue, M. Yan, Y.-X. Yin, Y.-G. Guo, *Adv. Funct. Mater.* **2018**, *28*, 1707533.

[61] K. Suzuki, D. Kato, K. Hara, T.-A. Yano, M. Hirayama, M. Hara, R. Kanno, *Electrochimica Acta.* **2017**, *258*, 110.

[62] H. Wu, Y. Huan, D. Wang, M. Li, X. Cheng, Z. Bai, P. Wu, W. Peng, R. Zhang, Z. Ji, M. Zou, X. Yan. *J. Electrochem. Soc.* **2019**, *166*, A188.

[63] Z. Cheng, Z. Xiao, H. Pan, S. Wang, R. Wang. *Adv. Energy Mater.* **2018**, *8*, 1702337.

[64] X. Liu, J.-Q. Huang, Q. Zhang, L. Mai, *Adv. Mater.* **2017**, *29*, 1601759.

[65] X. Chen, G. Du, M. Zhang, A. Kalam, S. Ding, Q. Su, B. Xu, A. G. Al-Schemi. *Energy Technol*. **2020**, *8*, 1901163.

[66] P. Long, Q. Xu, G. Peng, X. Yao, X. Xu, *ChemElectroChem.* **2016**, *3*, 764.

[67] Q. Zhang, X. Yao, J. P. Mwizerwa, N. Huang, H. Wan, Z. Huang, X. Xu, *Solid State Ionics.* **2018**, *318*, 60.

[68] X. Rui, H. Tan, Q. Yan, *Nanoscale.* **2014**, *6*, 9889.

[69] U. Ulissi, S. Ito, S. M. Hosseini, A. Varzi, Y. Aihara, S. Passerini, *Adv. Energy Mater.* **2018**, *8*, 1801462.

[70] Q. Ji, C. Li, J. Wang, J. Niu, Y. Gong, Z. Zhang, Q. Fang, Y. Zhang, J. Shi, L. Liao, X. Wu, L. Gu, Z. Liu, Y. Zhang, *Nano Lett.* **2017**, *17*, 4908.

[71] Y. J, Z. Zhou, C. R. Cabrera, Z. Chen, *J. Phys. Chem. C.* **2013**, *117*, 25409.

[72] M. Salavati, T. Rabczuk, *Comput. Mater. Sci.* **2019**, *160*, 360.

[73] L. Cai, Q. Zhang, J. P. Mwizerwa, H. Wan, Z. Yang, X. Xu, X. Yao, *ACS Appl. Mater. Interfaces.* **2018**, *10*, 10053.

[74] S. Xu, C. Y. Kwok, L. Zhou, Z. Zhang, I. Kochetkov, L. F. Nazar, *Adv. Funct Mater.* **2021,** *31*, 2004239.

[75] K. Takada, N. Aotani, K. Iwamoto, S. Kondo, *Solid State Ionics.* **1996**, *86*, 877.

[76] H. Zhang, L.-M. Liu, W.-M. Lau. *J. Mater. Chem. A.* **2013**, *1*, 10821.

[77] Z. Liu, W. Fu, E. A. Payzant, X. Yu, Z. Wu, N. J. Dudney, J. Kiggans, K. Hong, A. J. Rondinone, C. Liang, *J. Am. Chem. Soc.* **2013**, *135*, 975.

[78] Y. Yang, Q. Wu, Y. Cui, Y. Chen, S. Shi, R.-Z. Wang, H. Yan, *ACS. Appl. Mater. Interfaces.* **2016**, *8*, 25229.

[79] P. Atkins, T. Overton, J. Rourke, M. Weller, F. Armstrong, *Shriver & Atkins' Inorganic Chemistry 5th Ed.* Oxford University Press, Oxford, United Kingdom **2010**, 629.

[80] A. Sakurada, A. Hayashi, M. Tatsumisago, *Chem. Mater.* **2010**, *22*, 949.

[81] B. Wu, S. Wang, W. J. Evans, D. Z. Deng, J. Yang, J. Xiao, *J. Mater. A.* **2016**, *4*, 15266.

[82] J. Haruyama, K. Sodeyama, L. Han, K. Takada, Y. Tateyama, *Chem. Mater.* **2014**, *26*, 4248.

[83] W. D. Richards, L. J. Miara, Y. Wang, J. C. Kim, G. Ceder, *Chem. Mater.* **2016**, *28*, 266.

[84] Y. Aihara, S. Ito, R. Omoda, T. Yamada, S. Fujiki, T. Watanabe, Y. Park, S. Doo, *Front. Energy Res.* **2016**, *4*, 18.

[85] W. D. Richards, L. J. Miara, Y. Wang, J. C. Kim, G. Ceder, *Chem. Mater.* **2016**, *28*, 266.

[86] Y. Zhu, X. He, Y. Mo, *J. Mater. Chem. A.* **2016**, *4*, 3253.

[87] C. Y. Kwok, Q. Pang, A. Worku, X. Liang, M. Gauthier, and L. F. Nazar, *ACS Appl. Mater. Interfaces* **2019,** *11*, 22481.

[88] R. Xu, J. Yue, S. Liu, J. Tu, F. Han, P. Liu, C. Wang, *ACS Energy Lett.* **2019**, *4*, 1073.

[89] C. Chen, J. Jiang, W. He, W. Lei, Q. Hao, X. Zhang, *Adv. Funct. Mater.* **2020**, *30*, 1909469.

[90] T. Hakari, A. Hayashi, M. Tatsumisago, *Adv. Sustain. Syst.* **2017**, *1*, 1700017.

[91] K. Suzuki, N. Mashimo, Y. Ikeda, Y. Yokoi, M. Mirayama, R. Kanno, *ACS Appl. Energy Mater.* **2018**, *1*, 2373.

[92] M. Chen, S. Adams, *J. Solid State Electrochem.* **2015**, *19*, 697.

[93] M. Nagao, K. Suzuki, Y. Imade, M. Tateshi, R. Watanabe, T. Yokoi, M. Hirayama, T. Tatsumi, R. Kanno, *J. Power Sources.* **2016**, *330*, 120.

[94] X. Yang, J. Luo, X Sun, *Chem. Soc. Rev*. **2020**, *49*, 2140.

[95] X. Gao, *et. al*. *Nano Lett*. **2020**, *20*, 5496.

[96] R. R. Chianelli, M. B. Dines, *Inorg. Chem.* **1978,** *17*, 2758.

[97] P. Adeli, J. D Bazak, K. H. Park, I. Kochetkov, A. Huq, G. R. Goward, L. F. Nazar, *Angew. Chem. Int. Ed.* **2019**, *58*, 8681.

[98] K. Yuan, L. Yuan, Y. Liao, Z. Li, Y. Huang, *Small Structures.* **2020**, *2*, 200059.

[99] M. Kohl, J. Brückner, I. Bauer, H. Althues, S. Kaskel, *J. Mater. Chem. A.* **2015**, *3*, 16307.

[100] Y. Wu. *et. al. J. Electrochem. Soc.* **2020**, *167*, 020531